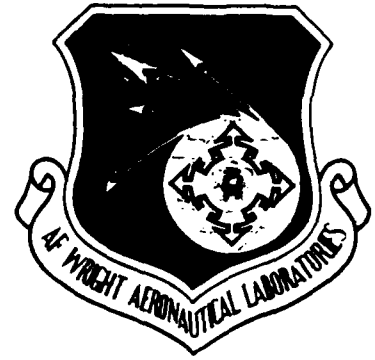


MICROCOPY RESOLUTION TEST CHART
NATIONAL BUREAU OF STANDARDS-1963-A

DTIC FILE COPY

2

AFWAL-TR-86-3072



NUMERICAL SIMULATION OF X24C-10D

AD-A183 287

Joseph J. S. Shang
Stephen J. Scherr

DTIC
ELECTE
AUG 12 1987
S CD D

June 1987

Final Report for Period June 1984 to July 1985

Approved for public release; distribution unlimited.

FLIGHT DYNAMICS LABORATORY
AIR FORCE WRIGHT AERONAUTICAL LABORATORIES
AIR FORCE SYSTEMS COMMAND
WRIGHT-PATTERSON AIR FORCE BASE, OHIO 45433-6553

87 7 28 198

A183287

REPORT DOCUMENTATION PAGE

1a. REPORT SECURITY CLASSIFICATION UNCLASSIFIED		1b. RESTRICTIVE MARKINGS	
2a. SECURITY CLASSIFICATION AUTHORITY		3. DISTRIBUTION/AVAILABILITY OF REPORT Approved for public release; distribution unlimited.	
2b. DECLASSIFICATION/DOWNGRADING SCHEDULE		4. PERFORMING ORGANIZATION REPORT NUMBER(S) AFWAL-TR-86-3072	
4. PERFORMING ORGANIZATION REPORT NUMBER(S) AFWAL-TR-86-3072		5. MONITORING ORGANIZATION REPORT NUMBER(S)	
6a. NAME OF PERFORMING ORGANIZATION Air Force Wright Aeronautical Laboratories	6b. OFFICE SYMBOL (If applicable) AFWAL/FIMM	7a. NAME OF MONITORING ORGANIZATION	
6c. ADDRESS (City, State and ZIP Code) AFWAL/FIMM Wright-Patterson AFB, OH 45433-6553		7b. ADDRESS (City, State and ZIP Code)	
8a. NAME OF FUNDING/SPONSORING ORGANIZATION	8b. OFFICE SYMBOL (If applicable)	9. PROCUREMENT INSTRUMENT IDENTIFICATION NUMBER	
8c. ADDRESS (City, State and ZIP Code)		10. SOURCE OF FUNDING NOS.	
		PROGRAM ELEMENT NO	PROJECT NO
		616100	2307
		TASK NO	WORK UNIT NO
		N6	11
11. TITLE (Include Security Classification) Numerical Simulation of X24C-10D			
12. PERSONAL AUTHOR(S) J.S. SHANG and S.J. SCHERR			
13a. TYPE OF REPORT Final	13b. TIME COVERED FROM Jun 84 TO Jul 85	14. DATE OF REPORT (Yr. Mo. Day) 1987, June	15. PAGE COUNT 59
16. SUPPLEMENTARY NOTATION			
17. COSATI CODES		18. SUBJECT TERMS (Continue on reverse if necessary and identify by block number)	
FIELD	GROUP	SUB GR	
01	01		
19. ABSTRACT (Continue on reverse if necessary and identify by block number)			
<p>The present effort represents a first attempt of numerical simulation of the flow field around a complete aircraft configuration utilizing the Reynolds averaged Navier-Stokes equations. The numerical solution generated for the experimental aircraft concept X24C-10D at a Mach number of 5.95 not only exhibited accurate prediction of detailed flow properties but also of the integrated aerodynamic coefficients. In addition, the present analysis demonstrated that a page structure of data collected into cyclic blocks is an efficient and viable means for processing the Navier-Stokes equations on the CRAY T3E-22 computer with external memory device.</p>			
20. DISTRIBUTION/AVAILABILITY OF ABSTRACT UNCLASSIFIED/UNLIMITED <input checked="" type="checkbox"/> SAME AS RPT <input type="checkbox"/> DTIC USERS <input type="checkbox"/>		21. ABSTRACT SECURITY CLASSIFICATION UNCLASSIFIED	
22a. NAME OF RESPONSIBLE INDIVIDUAL Joseph J. S. Shang		22b. TELEPHONE NUMBER (Include Area Code) (513) 255-7127	22c. OFFICE SYMBOL AFWAL/FIMM

FOREWORD

This report is the result of research performed in the Computational Aerodynamics Group, Aerodynamics and Airframe Branch, Aeromechanics Division, Flight Dynamics Laboratory from June 1984 to July 1985. This report was prepared by Dr Joseph J. S. Shang and Mr Stephen J. Scherr, under Work Unit 2307N611, "Computational Fluid Dynamics."

Two separated presentations to the American Institution of Aeronautics and Astronautics Scientific Meeting were derived from this effort. These presentations are entitled "Navier-Stokes Solution of the Flow Field Around a Complete Aircraft," AIAA 85-0159-CP and "Three-Dimensional Body-Fitted Grid System for a Complete Aircraft," AIAA 86-0428 respectively.

Accession For	
NTIS CR&I	<input checked="" type="checkbox"/>
DTIC TAB	<input type="checkbox"/>
Unannounced	<input type="checkbox"/>
Justification	
By	
Distribution/	
Availability Codes	
Dist	Avail and/or Special
A-1	



TABLE OF CONTENTS

<u>SECTION</u>		<u>PAGE</u>
I	INTRODUCTION	1
II	GOVERNING EQUATIONS	3
III	NUMERICAL PROCEDURE	6
IV	DISCUSSION OF NUMERICAL RESULTS	10
V	POST PROCESSING	14
VI	CONCLUSIONS	21
	ACKNOWLEDGMENTS	21
	REFERENCES	22
	APPENDIX A	
	Construction of the Grid System	25
	Hyperbolic Grid Generation	25
	Composite Grid Structure	28
	Spherical Grid at the Vehicle Nose	31

LIST OF ILLUSTRATIONS

<u>FIGURE</u>		<u>PAGE</u>
1	X24C-10D Configuration	33
2	Data Structure and Data Flow	34
3	Peripheral Surface Pressure Distributions of the Forebody	35
4	Peripheral Surface Pressure Distributions of the Afterbody	36
5	Surface Pressure Distribution on the Central Fin	37
6	Comparison with Pitot Pressure Survey ($X/R_n = 108.0$)	38
7	Peripheral Heat Transfer Distributions	39
8	Comparison of Surface Pressure Distributions at $X/R_n = 108.0$	40
9	Comparison of Heat Transfer at $X/R_n = 108.0$	41
10	Comparison of Streamwise Surface Pressure Distributions	42
11	Surface Pressure Contour	43
12	Surface Heat Transfer Contours	44
13	Cross-Sectional Mach Number Contours	45
13	Cross-Sectional Mach Number Contours (concluded)	46
14	Mach Number Contour Projected on the Plane of Symmetry	47
15	Surface Streamline Pattern	48
16	Composited Grid Structure by Hyperbolic and Trans-Finite Schemes	49
17	Typical Grid Systems in Selected Planes	50
18	Detailed Grid Construction in the Nose Region	51

LIST OF SYMBOLS

A	Reference area for aerodynamic force coefficient, 1303.2cm^2
C_D	Drag coefficient, $2D/\rho_\infty U_\infty^2 A$
C_L	Lift coefficient, $2L/\rho_\infty U_\infty^2 A$
C_p	Specific heat at constant pressure
e	Specific internal energy, $C_v T + 0.5(u^2 + v^2 + w^2)$
F, G, H	Flux vectors of conservation equations
H_∞	Stagnation enthalpy of the freestream
h	Enthalpy
I	Identity matrix
i, j, k	Unit vectors in Cartesian frame
M	Mach number
n	Surface outward normal
p	Static pressure
Pr	Molecular Prandtl number
Pr_t	Turbulent Prandtl number
q	Rate of heat transfer, $q = -k7t$
r_N	Radius of the blunt nose, 0.4826 cm
Re _y	Reynolds number
St	Stanton number, equation 12
t	Time
T	Temperature
u, v, w	Velocity components in the Cartesian frame
U	Dependent variables $U(\rho, \rho u, \rho v, \rho w, \rho e)$
x, y, z	Coordinates of the Cartesian frame
γ	Specific heat ratio
ϵ	Eddy viscosity coefficient

LIST OF SYMBOLS
(continued)

ξ, η, ζ Transformed coordinates
 μ Molecular viscosity coefficient
 ρ Density
 τ Stress tensor

Subscripts

∞ Freestream condition
 o Stagnation condition
 w Surface condition

Superscript

T Transpose of

I. INTRODUCTION

A continual and systematic progression of path-finding research in solving the Navier-Stokes equations has paved the way for the first attempt to simulate numerically the flow field around a complete aircraft.¹⁻⁴ In the present investigation, the hypersonic research aircraft X24C-10D is selected for its rather complex blunt leading edges, canopy, strake, fin and wing formations which are typical of those encountered in a modern aerospace vehicle (Figure 1). For the chosen aircraft, a detailed experimental data base also exists, in the form of a flow field pitot pressure survey, surface pressure, heat transfer, force and moment measurements.^{5,6,7} This experimental data establishes a solid criterion for assessment of the accuracy of the simulation. The validating comparison reveals technological emphases and research opportunities for our further endeavors in computational aerodynamics.

In principle, a composite solution using varying degrees of simplification of the Reynolds averaged Navier-Stokes equations for the flow field around a complete aircraft is possible. However, prior knowledge or unique insight into the flow field^{8,9} structure is required to implement this zonal approach. Additional evaluations of accuracy for each zonal solution and the boundary conditions for contiguous zones become necessary. As a benchmark calculation, the uncertainty is completely removed by seeking a solution of the Reynolds averaged Navier-Stokes equations. In order to depict adequately the investigated aircraft configuration, a mesh system consisting of 475,200 nodes was adopted. At present, processing and managing this huge amount of data requires a very large-scale vector processor with an external storage device. Therefore, a major portion of the present study is concentrated on the adaptation of our computational

procedure to the CRAY XMP-72 vector processor with a 16 million word MOS memory unit, the solid state storage device (SSD). In essence, the adaptation of a numerical procedure to a very large-scale computer comprises construction of a data base according to the computer architecture, and implementation of the procedure so as to minimize data movement.^{1,3} This is the first consideration so that one can extract the maximum data processing efficiency from a vector processor.

In order to achieve the stated objective, a careful matching of grid-point system, numerical algorithm and computer architecture is essential. Since there are no sharp leading edges in the investigated configuration, a composite grid system specially designed for high local numerical resolution is unnecessary.⁴ A single surface clustered body-conformal grid system is sufficient to facilitate the aerodynamic force calculations. The adopted MacCormack explicit, unsplit algorithm¹⁰ is known to advance in time with the minimum number of data accesses and has attained extremely high vector efficiency by continual improvement.^{1,3} Most importantly, the stencil of this algorithm requires no more than four contiguous nodes to be processed simultaneously in any given coordinate. This feature leads naturally to a page structure in grid point system construction, and eliminates the need for interface boundary conditions or repetitious regrouping of data to accomplish a particular orientation for a numerical sweep.¹¹ Finally, the minimum amount of data flow between the external memory unit SSD, and the central processor is obtained by partitioning the data into separated blocks sized according to the maximum number of data pages which can be accommodated in core memory. These data blocks will be cyclically rotated into the central processing unit as required by the numerical sweeps for convergence.

The numerical simulation was performed for the flow field around the entire aircraft at an angle of attack of six degrees with a nominal Mach number of 5.95 and the characteristic Reynolds number of 16.4 million/m. The benchmark numerical results will first be evaluated for accuracy in practical applications by prediction of the surface pressure distributions, the shock-wave structure, the heat transfer, the surface shear stress pattern, and the integrated aerodynamic force coefficients whenever comparison data are available. Since the entire flow field structure is reconstructed by the numerical simulation, the pertinent characteristics of the stream around various components of the aircraft are identified and highlighted for further investigations. These include the flows around the canopy, the swept-back blunt fins, and the induced vortex dominated stream in the lee of the aircraft. Then the overall numerical procedure is assessed for its relative efficiency, practical application value, and the areas of emphasis for future aerodynamics research.

II. GOVERNING EQUATIONS

The three-dimensional, compressible, Reynolds averaged Navier-Stokes equations in chain-rule conservative form are given as¹

$$\begin{aligned}
 & \frac{\partial U}{\partial t} + (\xi_x, \xi_y, \xi_z) \left(\frac{\partial F}{\partial \xi}, \frac{\partial G}{\partial \xi}, \frac{\partial H}{\partial \xi} \right)^T \\
 & + (\eta_x, \eta_y, \eta_z) \left(\frac{\partial F}{\partial \eta}, \frac{\partial G}{\partial \eta}, \frac{\partial H}{\partial \eta} \right)^T \\
 & + (\zeta_x, \zeta_y, \zeta_z) \left(\frac{\partial F}{\partial \zeta}, \frac{\partial G}{\partial \zeta}, \frac{\partial H}{\partial \zeta} \right)^T = 0
 \end{aligned} \tag{1}$$

It is easily identifiable that the dependent variable, U consists of $\rho, \bar{\rho u}$ and ρe

$$U = U(\rho, \rho u, \rho v, \rho w, \rho e) \tag{2}$$

The flux vectors, F, G, and H are simply the components of vectorial quantities of the continuity and energy equations, as well as the tensorial components of the momentum equations contained within the divergence operator of the conservation law.¹

The closure of this system of equations is obtained by including the Baldwin-Lomax turbulence model¹² for the Reynolds stress tensor and by assigning a turbulent Prandtl number with a value of 0.9 for the heat flux,

$$\bar{\tau} = - [p + 2/3(\mu+\epsilon)\nabla\cdot\bar{u}]\bar{I} + (\mu+\epsilon) \text{def } \bar{u} \quad (3)$$

$$\bar{q} = - \left(\frac{c_p \mu}{Pr} + \frac{c_p \epsilon}{Pr_t} \right) \nabla T \quad (4)$$

as well as the equation of state for a perfect gas and Sutherland's formula for the molecular viscosity coefficient. The description of this differential system of equations is completed, once the appropriate and well-posed initial and boundary conditions are specified.

In the present analysis we have taken advantage of the no-yaw flight condition, requiring only half of the configuration be computed with respect to the plane of symmetry. This simplification applied together with the idea of analytic continuation results in the leading coordinate surface ($\xi=0$) at the blunt nose becoming a developable surface by reflection. In practice, the grid system is constructed by overlapping two initial data pages in the ξ coordinate. The only constraints to achieve this topological requirement are that the basic cylindrical coordinates must transform into a spherical system near the blunt nose region and the number of peripheral nodes defining the surface must be an even integer. However, the latter constraint is imposed only for the purpose of convenience. In this manner, the adopted grid system is body conformal and simply connected, and the entire computational domain can be mapped into a unit cube. Details of the

construction of the mesh system, including the topology definition and the grid generation procedure, may be found in an accompanying paper¹³ and in Appendix A. In the transformed space, the initial and boundary conditions are summarized as follows:

Initial Condition

$$U(0, \xi, \eta, \zeta) = U_{\infty} \quad (5)$$

The $\xi=0$ surface is purely a numerical boundary created by the grid system. Since the two initial data pages in ξ are mirror images, the boundary values will be updated automatically. The $\xi=1$ surface represents the downstream boundary. The extrapolation condition is commonly used

$$\left. \frac{\partial U}{\partial \xi} \right|_{\xi=1} = 0 \quad (6)$$

On the body surface, $\eta=0$, the no-slip condition for velocity components and the surface temperature duplicating the experimental condition are given. The value of density on the solid contour is derived from the isobaric condition normal to the surface.

$$u=v=w=0 \quad (7)$$

$$T_w = 316.7^\circ\text{k} \quad (8)$$

and

$$\bar{n} \cdot \nabla p = 0 \quad (9)$$

where \bar{n} is the $\eta=0$ surface outward normal

$$\bar{n} = \frac{\eta_x \hat{i} + \eta_y \hat{j} + \eta_z \hat{k}}{\sqrt{\eta_x^2 + \eta_y^2 + \eta_z^2}}$$

$\hat{i}, \hat{j}, \hat{k}$ denote the unit vectors in the fundamental Cartesian frame. The far field boundary has transformed into the $\eta=1$ surface. This boundary is

located outside the enveloping bow shock wave system, where the flow retains the unperturbed freestream value

$$U = U_{\infty} \quad (10)$$

The $\zeta=0$ and $\zeta=1$ surfaces lay across the plane of symmetry. The condition of symmetry prevails

$$\frac{\partial U}{\partial \zeta} = 0 \quad (11)$$

III. NUMERICAL PROCEDURE

All calculations were performed on a CRAY XMP-22 vector processor with a 16 million word MOS memory unit, the solid-state storage device (SSD). The SSD appears logically as a disk drive with random-access storage. For reasons of efficiency, at present its operational configuration is limited to non-multi-tasked applications (no parallel processing). Therefore, only one central processor unit of nearly one million words of external memory was available. A mesh system consisting of 475,200 nodes was utilized to depict the complete aircraft configuration. Specifically, one hundred ten (110) nodes were assigned to define the cross-section of the aircraft in one hundred twenty (120) streamwise stations. Thirty-six (36) nodes were used to accommodate the computational domain bounded by the solid contours and far field. In short, a (110, 36, 120) mesh point system was adopted. In the present code, only five dependent variables $U(\rho, \rho \bar{u}, \rho e)$, three independent variables x, y, z and the eddy viscosity coefficient required permanent storage. The predictor level of dependent variables and nine components of the coordinate transformation derivatives are generated as needed. Therefore, the maximum amount of external data storage is 4,276,800 words.

MacCormack's explicit, unsplit algorithm vectorizes easily with ample opportunities for chaining operations. This reliable, conditionally

MacCormack's explicit, unsplit algorithm vectorizes easily with ample opportunities for chaining operations. This reliable, conditionally stable scheme, when incorporated with a time-warp acceleration procedure has demonstrated efficiency gains of a factor of six or more for solutions which possess a steady-state asymptote.^{1,14} For this explicit algorithm, only four contiguous nodes in any given direction are required to be processed simultaneously, the fourth node of data being included to support the fourth-order smoothing terms. The stencil permits a streamwise page structure of data in contrast to that of an implicit scheme which requires alternating structures of the data array to support differing orientation of numerical sweeps. For the aforementioned stencil, one detects that only the four cyclic predictor pages currently in use are required to be retained. The predictor and corrector sequence can be performed within one sweep by lagging the corrector calculation by two spatial pages. The coordinate transformation derivatives are repeatedly generated by a three-point, second order differencing scheme as needed without allocating a permanent storage space. Those additional arithmetic operations substantially reduce memory requirements but yield an in-core data processing rate of 3.077×10^{-5} seconds per iteration per node point.

In essence, computation of the three-dimensional Reynolds averaged Navier-Stokes equations becomes an intensive data transfer procedure between the central processor unit (CPU) and the data storage device (SSD). For the utilized computing system, the most efficient transfer rate for intermediate size data sets is around a half-million words (670 million bits per second). However, in the present investigation, one hundred twenty (120) streamwise stations were divided into twenty data blocks of six pages each. The minimum bandwidth which can support the four page data base is the six-page block. The additional two pages provide the coordinate

transformation derivatives at the four-page data interfaces. Each block of data was assigned a data set of 213,840 words. Two blocks, or twelve pages of data, were simultaneously resident in the CPU during the numerical sweep between the upstream and the downstream boundaries (Fig. 2). The rest of the in-core memory space was taken up by the temporary dependent variable arrays and the coding instruction. Individual data blocks were rotated into the CPU in sequence as required by the two-page lagging cycle of predictor-corrector procedure. In essence, the computer code serves as a data manager to control the four-page predictor-corrector cycle and the twelve-page external storage rotation. A measure of the relative efficiency for adaption of numerical procedure to a very large computer with an external memory device is the degradation of the data processing rate (DPR) in comparison with in-core performance. For the present investigation, a total of 4,276,800 words processed by a 880,000 word CPU, the degradation is less than 23 percent in DPR. The data processing rate in conjunction with the SSD is consistently 3.7814×10^{-5} seconds per iteration per grid point.

As a pleasant surprise, the page and block data structure has been demonstrated to reduce the required computing time for overall convergence. Due to the numerical sweep bias, the upstream numerical simulation tends to converge sooner than that of the downstream. As the data converged in an upstream block need not be rotated into the CPU, the total number of data blocks can be truncated accordingly. A net saving in computing time of up to thirty percent has been realized by suppressing unnecessary calculation in the converged region. Computation performed for this truncated domain is effectively equivalent to a zonal method, but has no need of explicit zonal boundary conditions.

For the numerical simulation of a complete aircraft, the surface normal grid spacing required to resolve the shear stress or heat transfer can no longer be gauged by a single selected value of the law of the wall variable, y^+ . Consideration must be given to the large upstream ratio between normal and peripheral mesh size and the growth rate of the boundary layer along the entire configuration. From two different estimates of the laminar sublayer thickness based upon a turbulent boundary layer scaling law, the minimum surface normal step size was determined to be 9.1×10^{-3} cm. This nominal value was used as a guide to set an appropriate overall grid spacing and a finer mesh step in the nose region, where the surface normal step size is a factor 4.09 time finer than the nominal value. The peripheral node distribution is weighted by the local radius of curvature. The resulting stretching is relatively limited in magnitude, generally confined within a fraction of a basic unit. However, in the streamwise direction, the ratio between the maximum and the minimum step size is as high as 19.47. The high grid density zones were concentrated around the nose region and the locations where the canopy, strake and fin protrude into the incoming stream. The hundred twenty pages are nearly equally divided between the forebody and the afterbody. Analysis of the flow field immediately downstream of the blunt nose through the emergence of the strake by a parabolized Navier-Stokes scheme^{8,9} indicated that the maximum grid spacing could be used in this region. The assigned value was 1.46 cm. Finally, the steady asymptote of the numerical solution is considered to be reached when the L_1 norm between two consecutive normalized pressure values is less than 10^{-5} . This criterion is much less stringent than the evaluation of heat transfer and is considered suitable for our present purpose.

IV. DISCUSSION OF NUMERICAL RESULTS

The discussion of results comprises two major portions. The first group of presentations is accompanied by experimental measurements of shock structure, and heat transfer data.^{5,6} Then a specific comparison with a numerical solution of the parabolized Navier-Stokes equations for the forebody is presented and discussed. Observations on the characteristics of flow observed from the numerical simulation will also be delineated to identify areas of future research emphasis.

Since most of the experimental measurements were collected at several predetermined streamwise stations, the format of comparison is constructed accordingly. Typical results are given by abscissas in the form of the normalized arc length. This length is computed from the leeward meridional plane toward the windward counterpart and scaled by the total arc length of each individual cross section. In Figure 3 and Figure 4 a total of eleven streamwise stations are depicted. These stations represent a sequential evolution from the blunt nose region until the trailing section. The physical locations span a range of 15 to 141.25 radii from the coordinate origin which is 3.35 radii upstream of the blunt nose, $r_N = .483$ cm. The overall agreement between data and numerical results is excellent. In Figure 5, the streamwise compression and its subsequent expansion around the canopy due to the recessed and flattened out leeward surface are obvious. In each cross-sectional plane, the expansion from windward to leeward domains stands out. The surface pressure distributions also exhibit a relatively rapid compression at the lower corner of the trapezoidal cross section. This local phenomenon bears a strong resemblance to that of the blunt leading edge of a delta wing. The surface pressure distributions of the afterbody are given by Figure 6. Each pressure spike represents the

result of protruding fins or strake into the oncoming stream. The pressure distribution reveals the emergence of the central fin near the origin of abscissas, the middle fin, and the strake from the afterbody. Finally, the strake, due to recession, ceases to be an exposed blunt edge ($x/r = 141.25$). Unfortunately, the $x/r = 125.75$ station has the only two pressure taps installed on the leading edge of the strake. The accordance between the data and numerical results is excellent.

Figure 5, three pressure distributions around the central fin at different elevations ($z/r = 20, 25, 30$) are given. These elevations correspond to distances of 0.92 cm, 3.33 cm, and 5.74 cm above the upper model surface.⁵ The collapsing of all pressure distributions into a narrow band reveals that in spite of all upstream disturbances, the leeward flow field immediately surrounding the central fin remains nearly uniform at this moderate angle of attack. The maximum deviation between data and calculations is limited to a few percent.

The flow field survey data by pitot pressure probes⁶ is presented together with the computed impact pressure contour in Figure 6. It is clearly exhibited that the numerical simulation duplicates the measurements. The definition of the shock wave system as captured by the numerical mean is comparable to the data scattering band.⁶ As we have mentioned earlier, the enveloping shock wave system has attenuated substantially in the leeward region to be detected as a Mach wave.

In Figure 7, the heat transfer in form of Stanton number distributions in five streamwise stations ($x/r = 108, 117, 125, 131.50, 141.25$) are depicted. These data collecting stations are identical to those of the surface pressure in the afterbody region. The Stanton number is defined by

$$St = \dot{q}_w / \rho_\infty u_\infty (H_\infty - h_w) \quad (12)$$

The numerical value of the rate of heat transfer was computed directly from the profiles of specific internal energy instead of static temperature to take advantage of the monotonic distribution of the former adjacent to the body surface. The specific formula used is

$$St = \frac{\gamma \mu_w}{Pr} (\eta_x^2 + \eta_y^2 + \eta_z^2)^{1/2} \frac{\partial}{\partial \eta} (\rho e / \rho) / [\rho_w u_w (H_e - h_w)] \quad (13)$$

The coordinate transformation derivatives are included as a consequence of obtaining the heat flux normal to the body surface, $\bar{q} = \bar{n} \cdot \bar{q}$. The overall comparison between data and computational results is only fair. The peak heating is consistently concentrated around the exposed blunt leading edge of the fins and strake. Since no thermocouple could be installed at these leading edges because of their size, a verification by the analytic solution based upon the reference temperature method for the stagnation point was performed.¹⁶ The analytic solution yielded a Stanton number of 1.243×10^{-2} which is within ten percent (10%) of the numerical prediction locally. However, the persistent and maximum discrepancy (20%) between data and the present calculations is located on the windward surface and over a wide range of the streamwise stations.¹⁷ This behavior has been commonly detected in numerical simulations of flow fields with incidence. Although the local grid density is relatively high, the maximum normal grid spacing does not contract according to the compressed boundary layer thickness. This observation leads logically to the speculation that further grid refinement is probably more critical than the improvement of the turbulence model. A single effort in this research area would yield some invaluable basic knowledge. In all, the present calculations follow the trend of data in revealing the peak heating of the exposed leading edges and troughs of heat transfer induced by the separated and incipient separation zones on the leeward surface and corner regions between fins.

A series of remarkable numerical solutions using the parabolized Navier-Stokes equations has been performed for the forebody of the investigated complete configuration by Chaussee et al.^{8,9} Their composite numerical procedure initiated a full Navier-Stokes solution for the blunt nose region which served as the initial boundary condition of the subsequent space-marching solution until the strake, then the solution was terminated. Their experience suggested a very coarse streamwise step size was permissible between the canopy and the beginning of the strake. Therefore, only twenty one (21) streamwise stations and the coarsest mesh spacing ($\Delta x = 1.45$ cm) were implemented within this region for the present investigation.

Surface pressure and the Stanton number distribution comparisons with the parabolized Navier-Stokes solutions at their furthest downstream station ($x/r = 108$) are presented in Figures 8 and 9 respectively. The agreement in surface pressure distribution is very good. However, the presence of upstream pressure propagation due to the strake is detectable in the present computation. The small difference between numerical solutions is therefore attributable to the omitted interaction in PNS solution for the protrusion of the strake. The difference in the heat transfer data is more noticeable in the leeward surface beneath the roll-up of the vortex. Perfect accordance is reached on the windward surface and both numerical values under-predict the experimental measurement. The strong dependence on grid systems adopted in the PNS calculations was reported.⁹ In order to avoid confusion, only data from the cylindrical coordinate system generated by a hyperbolic procedure (which give the best agreement with the experimental data) is included here for comparison.

The windward and leeward pressure distributions along the plane of symmetry are given by Figure 10. The outstanding feature is clearly that

for a hypersonic lifting configuration the surface pressure varies in magnitude over several orders. In the nose region, the pressure attains the maximum value of 41.8 times of the freestream; the minimum value is only about 0.05 times of the unperturbed value in the corners between fins. The windward pressure distribution indicates the rapid expansion from the stagnation point and maintains a gradual compression throughout the windward surface until the expansion initiated at the trailing boattail. The leeward surface pressure undergoes expansion from the nose, recompresses over the canopy followed by the expansion and finally rises over the central fin. The agreement between the parabolized Navier-Stokes solution⁹ and the present result is very good for the forebody, excepting perhaps some mild fairing which may have caused the underprediction of the pressure value over the canopy by the parabolized Navier-Stokes procedure. Only the comparison of present results and data is existing for the afterbody of the complete configuration. The overall agreement serves to validate the present effort and confirm the choice of grid spacing in the forebody region.

V. POST PROCESSING

In this section, a reconstruction of the entire flow field around the X24C-10D research aircraft is attempted to gain understanding of the salient features of its structure. The overall surface pressure distribution and heat transfer around the aircraft is given together with the immediately adjacent surface streamline to depict the surface shear stress pattern and to identify the possible separated flow regions. However, the graphic presentation of the flow field in form of Mach contours is limited to a few cross sections. Finally, the detailed numerical procedure used in evaluating the aerodynamic forces exerted on the aircraft is included. This

information is probably the most critical to the aircraft design and should be provided in the numerical simulation effort.

The overall surface pressure on the X24C-10D experimental aircraft is depicted in a perspective view in Figure 11. (Shang and Scherr plate 1). As we have mentioned previously, the value of surface pressure spans a range of several decades so an artificially compressed scale (cube root value of pressure) was used to span the pseudo color spectrum. As anticipated, the high pressure regions are easily recognizable around the nose, canopy, leading edges of strakes and fins the aircraft components exposed to the oncoming stream. The extensive expansion above the leeward surface downstream of the canopy is also apparent, but the lowest pressure level is confined to the inner fin root region of the middle fin. The evidence of interference on the middle fin, originating from the strake, is reflected by the intermittent high and low surface pressure value over the backward swept fin. This phenomenon is verified by the experimental data. One of the interesting revelations is that the pressure along the side surface of the fuselage is nearly constant until the afterbody contracts to form a recessed boattail where the flow expands toward the downstream. The recompression along the plane of symmetry to realign the orientation of vortical flow above the leeward surface is also clearly indicated.

The characteristics of heat transfer to the surface are depicted by the static temperature of the immediately adjacent nodes away from the surface (Figure 12, Shang and Scherr, plate 2). Since the body surface is maintained at a constant temperature, this local temperature effectively dictates the intensity of heat transfer to the solid surface. The high heating regions generally correspond to the exposed elements of the aircraft analogous to the surface pressure. However, secondary high heating zones are also indicated in the inviscid-viscous interacting regions surrounding

the canopy, adjacent to the plane of symmetry and the areas between strake and fins as well as the domain bounded by the fins. The only unusual patterns observed are the overexpansion of upwash leading to a lower heat transfer rate around the leeward outboard corner and continuing to the leading section of the strake where the afterbody recedes. All these observations are supported by the detailed calculations presented in the previous section of discussion.

The effort involved in a complete reconstruction of the entire flow field in a graphic presentation has proved to be prohibitive at present. The basic difficulty of two-dimensional projection of a three-dimensional phenomenon can, in principle, be overcome by a holographic stereogram. Unfortunately, the supporting facilities in long-haul communication and limited capacity of graphic work stations in simultaneous display of data still fall short. In order to exhibit the peculiar features of the investigated flow field, four cross-sectional Mach number contours are given in Figure 13 (Shang and Scherr, plate 3). At the streamwise station $x/r = 39.5$, the induced shock wave system over the canopy and the dispersion of the bow shock envelope over the leeward domain of this section of the forebody are apparent. At the last forebody cross section, the attenuation of the bow shock wave by the expansion from the windward to the leeward domain becomes very clear. The shock wave generated by the canopy by now is completely dispersed. Similarly, the vortical formation near the leeward plane of symmetry is also obvious, together with the induced higher Mach number pockets above and outboard of the vortices. At the next station downstream, $x/r = 125.63$, the bow shock wave enveloping the strake impinges on the middle fin and exhibits significant distortion in structure. This interference is observed persistently over the entire afterbody even

downstream of the location where the leading edge of the strake sweeps backward and parallel to the axis of symmetry of the afterbody. In the last cross sectional plane presented, $x/r = 145$. The bow shock wave originating from the blunt nose continues to exist in the windward domain. The enveloping bow shock waves over the fins and the strakes dominate the flow field. Even though the leading edge of the strake has turned parallel to the fuselage axis, its associated bow shock wave still retains sufficient strength to interact with the bow shock waves over the middle fin. Unfortunately, little detailed information is discernible by the relatively coarse supporting local mesh system. The bounding shock waves above the strakes are observed to merge with the bow shock wave generated by the blunt nose with attenuation around the lower fuselage convex corner. The bow shock wave over the central fin also interacts with the vortical structure in the fin root region. However, the interaction is rather limited in intensity and is confirmed by the collapsing surface pressure distributions around the central fin (Figure 5). It is also interesting to note that the high Mach number pockets induced by vortex and expansion still persist even to this streamwise station.

Mach number contours in the plane of symmetry are depicted in Figure 14 to serve as an additional cross reference. The bow shock wave system originating from the blunt nose is clearly identifiable. In the windward domain, the shock strength is maintained over the entire configuration. The expansion triggered by the retracted lower boattail surface is also revealed. In the leeward domain, the shock wave system induced by the canopy, its subsequent dispersion and the following bow shock waves over the central fin stand out. The envelope of the bow shock wave system projected on the plane of symmetry yields a total wave inclination of 22

degrees over the forebody. This value is in perfect accordance with the experimental observation by a shadowgraph.

The surface streamlines prepared by P. Buning of NASA Ames Research Center is presented in Figure 15. This approximate surface shear flow pattern is constructed by the first node velocity components away and parallel to the body surface. The upwash of the nose region due to the incidence and the secondary flow structure immediately upstream of the canopy are clearly revealed. The surface streamlines converging at the onset of the canopy and diverging over the canopy surface suggest a confined and small separated flow region embedded in the junction between canopy and fuselage. The low local heat transfer rate seems to confirm this observation. However, the separation and reattachment over the leeward surface downstream of the canopy is without any ambiguity. The surface streamlines also reveal tendencies to converge around the junctions of middle fin, strake and the afterbody implying incipient separation. The relatively low heat transfer distribution is in correspondence with this idea, but the topological constraints of the converging fins preclude a conclusive interpretation. An interesting observation can also be made on the lack of a horseshoe vortex structure around the blunt fins.¹⁷ This may be associated with the swept back configuration of fins. The drastic difference in flow field structure between the vertical blunt fin and the swept back fins may warrant a detailed and separate investigation.

The aerodynamic force exerted on the complete configuration can be easily derived from the Cauchy's theorem

$$\bar{F} = \bar{n} \cdot \bar{\tau} \quad (14)$$

where the stress tensor is given by

$$\bar{\tau} = \begin{vmatrix} \tau_{yx} & \tau_{xy} & \tau_{xz} \\ \tau_{yx} & \tau_{yy} & \tau_{yz} \\ \tau_{zx} & \tau_{zy} & \tau_{zz} \end{vmatrix}$$

The specific expression of the stress tensor has been shown in Equation (3) which contains the static pressure as a component of the normal stress. The net aerodynamic force components at a point on the control surface, $\eta =$ constant, in the Cartesian frame are

$$F_x = (\eta_x \tau_{xx} + \eta_y \tau_{xy} + \eta_z \tau_{xz}) / \sqrt{\eta_x^2 + \eta_y^2 + \eta_z^2} \quad (15a)$$

$$F_y = (\eta_x \tau_{xy} + \eta_y \tau_{yy} + \eta_z \tau_{yz}) / \sqrt{\eta_x^2 + \eta_y^2 + \eta_z^2} \quad (15b)$$

$$F_z = (\eta_x \tau_{xz} + \eta_y \tau_{yz} + \eta_z \tau_{zz}) / \sqrt{\eta_x^2 + \eta_y^2 + \eta_z^2} \quad (15c)$$

In the present investigation, the control surface coincides with the body surface. Since the present analysis omitted the base configuration, the trailing surface was not included in the computation. For a hypersonic vehicle, the drag contribution from the blunt nose and wave system should overwhelm that of the base regime. The present simplification will serve as a verification of this conjecture for engineering applications. However, the present formulation is derived to be independent of this approximation and to retain the general validity.

The surface integral of an arbitrary plane defined by $x(\xi, \zeta)$, $y(\xi, \zeta)$ and $z(\xi, \zeta)$ is¹⁶

$$\iint F_1(x, y, z) [(x_\xi^2 + y_\xi^2 + z_\xi^2)(x_\zeta^2 + y_\zeta^2 + z_\zeta^2) - (x_\xi x_\zeta + y_\xi y_\zeta + z_\xi z_\zeta)^2]^{1/2} d\xi d\zeta \quad (16)$$

The above expression can be further simplified by the definition of the Jacobian of the coordinate transformation and some algebraic manipulation to yield

$$\iint F_1(x,y,z) [(\eta_x^2 + \eta_y^2 + \eta_z^2)/J^2]^{1/2} d\xi d\zeta \quad (17)$$

Finally, we have the net aerodynamic force components exerted on the complete configuration

$$F_x = \iint (\eta_x \tau_{xx} + \eta_y \tau_{xy} + \eta_z \tau_{xz}) / |J| d\xi d\zeta \quad (18a)$$

$$F_y = \iint (\eta_x \tau_{yx} + \eta_y \tau_{yy} + \eta_z \tau_{yz}) / |J| d\xi d\zeta \quad (18b)$$

$$F_z = \iint (\eta_x \tau_{zx} + \eta_y \tau_{zy} + \eta_z \tau_{zz}) / |J| d\xi d\zeta \quad (18c)$$

where, the Jacobian of coordinate transformation is given by

$$J = \begin{vmatrix} \xi_x & \eta_x & \zeta_x \\ \xi_y & \eta_y & \zeta_y \\ \xi_z & \eta_z & \zeta_z \end{vmatrix}$$

The aerodynamic force components along any desired direction can be obtained by a simple projection.

In the present formulation, the advantage of a body conformal coordinate system is transparent. One recognizes the necessity of a zonal construction of the grid system for complex configurations, however, consideration should also be devoted to the ease of post processing.

The specific comparison of the computed drag and lift coefficients to the experimental data is presented in Table 1. The difference in lift coefficients is merely 4.72 percent and the drag coefficient has a discrepancy of 6.70 percent. However, the compensating errors in numerical

underprediction yields a L/D ratio within 2.16 percent of the experimental measurement. This agreement is confined within the accepted experimental error band. Indirectly, this comparison seems to justify the present omission of the base drag contribution.

VI. CONCLUSIONS

The first numerical simulation of the flow field around a complete aircraft, the hypersonic research aircraft X24C-10D, utilizing the Reynolds averaged Navier-Stokes equations has been accomplished, yielding accurate prediction of detailed flow properties. The numerical results obtained at a Mach number of 5.95 also indicate an excellent agreement in aerodynamic force coefficients with those of experimental data.

The page data structure collected into separated blocks and cyclically rotating from the external storage device into the central processor has been demonstrated as an efficient and viable adaptation of the numerical procedure to a very large class computers without sufficient dynamic memory. The cyclic data block structure has also been found to be a convergence enhancement device by selectively processing data according to its rate of convergence.

The parabolized Navier-Stokes solution generated for the forebody of this aircraft has been verified by the present result. A composite numerical procedure for the entire configuration may be desirable for efficiency improvement. Urgent research emphases still exist in continuing improvement of numerical efficiency, long-haul communication and graphic support of the computational aerodynamics discipline.

ACKNOWLEDGEMENTS

The authors would like to acknowledge the computer support supplied by NASA's Ames Research Center, the assistance with the hyperbolic grid

generator provided by Timothy J. Barth. The authors would also like to thank Miss Tammy L. Sutphin for her effort in preparing this manuscript.

REFERENCES

1. Shang, J.S., "An Assessment of Numerical Solutions of the Navier-Stokes Equations," AIAA Paper 84-1549, July 1984.
2. Shang, J.S. and Hankey, W.L., "Numerical Solution of the Navier-Stokes Equations for a Three-Dimensional Corner," AIAA Journal, Vol. 15, No. 11, November 1977, pp. 1575-1582.
3. Shang, J.S., Buning, P.G., Hankey, W.L. and Wirth, M.C., "Performance of a Vectorized Three-Dimensional Navier Stokes Code on the CRAY-1 Computer," AIAA Journal, Vol. 18, No. 9, September 1980, pp. 1073-1079.
4. Shang, J.S., "Numerical Simulation of Wing-Fuselage Aerodynamic Interaction," AIAA Journal, Vol. 22, No. 10, October 1984, pp. 1345-1353.
5. Wannernwetsch, G.D., "Pressure Tests of the AFFDL X-24C-10D Model at Mach Numbers of 1.5, 3.0, 5.0 and 6.0," AEDC-DR-76-92, Von Karman Gas Dynamics Facility, Arnold Engineering Development Center, TN, November 1976.
6. Carver, D.B., "AFFDL X24C Flowfield Survey," Von Karman Gas Dynamics Facility, Arnold Engineering Development Center, TN, Project No. V41B-47, June 1979.
7. Neumann, R.D., Patterson, J.L. and Sliski, N.J., "Aerodynamic Heating to the Hypersonic Research Aircraft X24C," AIAA Paper 78-37, 1978.
8. Chaussee, D.S., Patterson, J.L., Kutler, P., Pulliam, T.H. and Steger, J.L., "A Numerical Simulation of Hypersonic Viscous Flow over Arbitrary Geometries at High Angle of Attack," AIAA Paper 81-0050, January 1981.
9. Kaul, U.K. and Chaussee, D.S., "A Comparative Study of the Parabolized Navier-Stokes Code Using Various Grid-Generation Techniques," AIAA Paper 82-184, 1982.

10. MacCormack, R.W., "The Effect of Viscosity in Hypervelocity Impact Cratering," AIAA Paper 69-354, 1969.
11. Lomax, H. and Pulliam, T.H., "A Fully Implicit Factored Code for Computing Three-Dimensional Flows on the ILLIAC IV; Parallel Computations," ed. G. Rodrigue, Academic Press, NY, 1982, pp. 217-250.
12. Baldwin, B.W. and Lomax, H., "Thin Layer Approximation and Algebraic Model for Separated Turbulent Flows," AIAA Paper 78-257, January 1978.
13. Scheir, S.J. and Shang, J.S., "Three Dimensional, Body Fitted Grid System for a Complete Aircraft," Submitted to the AIAA 24th Aerospace Sciences Meeting.
14. Visbal, M. and Shang, J.S., "A Comparative Study Between an Implicit and Explicit Algorithm for Transonic Airfoils," AIAA Paper 85-0480, 1985.
15. Newsome, R.W., Jr., "A Comparison of Euler and Navier-Stokes Solutions for Supersonic Flow over a Conical Delta Wing," AIAA Paper 85-0111, January 1985.
16. Hayes, W.D. and Probstein, R.F., "Hypersonic Flow Theory," Academic Press, New York, 1959, pp. 292-303.
17. Hung, C.M. and Buning, P.G., "Simulation of Blunt-Fin Induced Shock Wave and Turbulent Boundary Layer Interaction," AIAA Paper 84-0457, January 1984.
18. Weinstock, R., "Calculus of Variations," McGraw-Hill Book Company, New York, 1952, pp. 11-12.
19. Steger, J. and Chaussee, D., "Generation of Body-Fitted Coordinates Using Hyperbolic Partial Differential Equations," SIAM J. Sci. Stat. Comput., Vol. 1, Dec 1980, pp. 431-437.
20. Kinsey, D.W. and Barth, T.J., "Description of a Hyperbolic Grid Generating Procedure for Arbitrary Two-Dimensional Bodies," AFWAL-TR-84-191-FIMM, July 1984.

21. **Beam, R.W. and Warming, R.P., "An Implicit Finite-Difference Algorithm for Hyperbolic Systems in Conservation Law Form," J. Comp. Phys. 12 (1976), pp. 87-110.**
22. **Vinokur, M., "On One-Dimensional Stretching Functions for Finite-Difference Calculations," NASA Contractor Report 3315, October 1980.**

TABLE 1

	ϵ_1	ϵ_D	ϵ_{FD}
Experimental Data	3.676×10^{-2}	3.173×10^{-2}	1.158
Numerical Result	3.503×10^{-2}	2.960×10^{-2}	1.183
Percent Error	4.71	6.71	2.16

APPENDIX A

Construction of the Grid System

The grid system was constructed in distinct regions which were then merged to form one computational block. The primary division was between the spherical grid at the vehicle nose and the cylindrical structure over the rest of the aircraft body. Each plane of the cylindrical system was further subdivided into three regions: a hyperbolic grid next to the body, and two transversely interpolated regions which continued the grid from the hyperbolic part to the prescribed outer boundary (Figure 16). This arrangement allowed all the conditions specified for the grid to be satisfied. The multiple-plane structure of the mesh system was conveniently implemented by letting a $\xi = \text{constant}$ plane also be an $x = \text{constant}$ plane. The grid was made orthogonal in each plane at the vehicle surface by use of a suitable hyperbolic grid generator. The restrictions on the outer portion of the mesh were satisfied by the creation of the composite structure. Smoothness of derivatives between regions of the grid was enhanced by application of a Poisson operator.

Hyperbolic Grid Generation

Orthogonality of the grid at the vehicle surface was the first requirement for the mesh system. This constraint was slightly relaxed to require only that it be orthogonal in each $x = \text{constant}$ cross section. This was guaranteed by use of a hyperbolic grid generation algorithm originally proposed by Steger and Chaussee¹⁹ and further modified by Kinsey and Barth.²⁰ This algorithm takes the definition of grid orthogonality

$$y_n y_\zeta + z_n z_\zeta = 0 \quad (1)$$

and the transformation Jacobian

$$y_n z_\zeta - y_\zeta z_n = 1/J \quad (2)$$

to devise a scheme mapping (y, z) to (r, t) . Locally linearizing about the point (y^*, z^*) and noting that an area integrand can be written $dV = dy dz / J \, d\eta \, d\zeta$, (1) and (2) become

$$AR_{\zeta} + BR_{\eta} = F$$

where $A = \begin{vmatrix} y_r^{\circ} & z_r^{\circ} \\ -z_{\eta}^{\circ} & +y_{\eta}^{\circ} \end{vmatrix}$, $B = \begin{vmatrix} y_{\zeta}^{\circ} & z_{\zeta}^{\circ} \\ +z_{\zeta}^{\circ} & -y_{\zeta}^{\circ} \end{vmatrix}$, $R = \begin{vmatrix} y \\ z \end{vmatrix}$, and

$$F = \begin{vmatrix} 0 \\ v+v^{\circ} \end{vmatrix}$$

Inspection of $B^{-1}A$ shows that this system is hyperbolic and can be marched in η .

The finite difference solution scheme of the original algorithm is centrally differenced in ζ and backward differenced in η . It can be written as

$$[I + B^{-1}A\delta_{\zeta}]R_{k,j+1} = R_{k,j} + B^{-1}F_{k,j+1} + \epsilon (v_k \delta_{\zeta})^2 k_{k,j}$$

where the final term adds explicit, fourth-order dissipation as described in Beam and Warming.¹⁵ To insure smoothness, additional temporal and spatial dissipation is added. Spatial dissipation comes from the use of a more general class of integration in η :

$$\frac{R_{j+1} - R_j}{\Delta\eta} = (1-\beta) \left(\frac{\partial R}{\partial \eta}\right)_j + \beta \left(\frac{\partial R}{\partial \eta}\right)_{j+1}$$

When $\beta=1$, the original backward differenced scheme is obtained. For $\beta < 1$, the error term has a dissipative effect in the η direction. Rewriting the algorithm in delta form and adding temporal dissipation through an implicit term, which does not formally degrade the accuracy of the algorithm, the

final form of the scheme is

$$[1 + \epsilon_1 (V_k \Delta_k)^2 + \beta B^{-1} A_0] (R_{j+1} - R_j) \sim B^{-1} [\beta V_{j+1}^* + (1-\beta) V_j] + \epsilon_e (V_k \Delta_k)^2 R_j$$

Note that this scheme requires the (2-dimensional) cell volumes at the j and $j+1$ levels. The j level volume can be computed from the existing grid in terms of the metric functions, using (2). The volume at $j+1$ is estimated by referring to an average of cell volumes from two idealized polar grids. Both these grids are formed about circles whose circumference equals the arc length of the body cross section and both have an exponential stretching in the radial direction. The polar grids vary in their spacing in the circumferential direction, one being equispaced and the other having spacing proportional to the original distribution of points on the body. The $j+1$ cell volume is chosen to transition smoothly from the corresponding volume in the unequally spaced grid, when the cell is at the body, to the volume in the equispaced grid, when the cell is far from the body.

The parameters have been used in generating the grid control dissipation, spacing, and orthogonality. β relaxes the orthogonality of the grid as f moves away from 1.0. This helps the grid to adapt to the wide variation in curvature of the body, without forcing it to kink or overlap itself. Orthogonality is forced at the body surface by setting the following parameters at $j=2$: $\beta=1.0$, $\epsilon_e=0.0$, and $\epsilon_1=0.0$. These parameters then increase linearly with j to their maximum value at $j=j_1$, and stay constant at that value. In order that the radial lines do not spiral back in toward the body, the value of β is returned to 1.0 between $j=j_1$ and j_{max} . The other values used to generate the hyperbolic grids were $\beta_{max}=1.0$, $(\epsilon_e)_{max}=0.05$, $(\epsilon_1)_{max}=0.048$, $j_1=8$, and $j_2=30$. The radial spacing at the wall was $0.0289 r_N$ and the nominal total radial distance, used in estimating cell volumes, was $25 r_N + 0.1(x-x_c)$.

The distribution of points on the body was controlled by use of arc length weighted by curvature. The hyperbolic grid generator marches the grid out from some predetermined body contour with some given point spacing. An existing program was used which, given an axial location x , would produce a sequence of points describing the body cross section at that particular station. The curvature, κ , was computed at each point and the weighted arc length, $S(s) = \int (1 + \lambda \frac{\max(\kappa, 0)}{\kappa_{\max}}) ds$ was calculated along the curve, where λ is a weighting factor for the curvature. Points were then placed on the curve so as to be equispaced in S . This function tends to cluster points at convex corners and give a uniform distribution along straight lines and at concave corners. This kind of clustering is that typically required in an external problem. It was also arranged that both end pairs of points would straddle the centerline of the body, for use in implementing the symmetry condition. The parameter λ was set to zero for $0 \leq x \leq 0.5$. This forced the points to be equispaced in arc length on the forebody. λ increased linearly with x to a value of 2.5 at $x = 1.0$ and remained at that level for $1.0 \leq x \leq 7.0$. It was hoped that this method of placing the points would lead to smooth changes between planes of the grid.

Composite Grid Structure

The second requirement on the mesh system was that it conform to a smooth outer boundary. An attempt was made to use varying cell volumes in the hyperbolic grid, these cell volumes being determined by fracturing the grid generator. This attempt was unsuccessful, as it led to a kinked boundary, and the implementation of the method proved to make control of the boundary too difficult. Thus, an alternate method was employed, using transfinite interpolation from a specified ϵ level of the hyperbolic grid through an intermediate smooth boundary and on to the desired outer boundary.

The analytic description of the outer boundary was formulated based on experimental results. A pitot pressure survey at the last forebody station ($x/r_N = 128.0$) indicated the presence of a bow shock wave of approximately bi-elliptical shape (Figure 6). A shadowgraph picture taken of the experimental model showed that the shock wave projection in windward domain grew linearly with x at an angle of $\theta = 13.5^\circ$. Thus, the outer boundary was defined to be a bi-elliptical shape centered at $(0,0)$ with y -axis length $A(x)/r_N = [32.5+(x-128.0 r_N) \tan\theta]\phi$, upper z -axis length $B_1(x)/r_N = [50+(x-128.0 r_N) \tan(\theta+\alpha)]\phi$, and lower z -axis length $B_2(x)/r_N = [17.5+(x-128.0 r_N) \tan(\theta-\alpha)]\phi$. The inclusion of the angle of attack, α , enables the grid generation program to have a wider range of applicability. The multiplicative factor $\phi=1.25$ increases the size of the grid to make certain that the entire bow shock is captured.

In order to match the cylindrical grid generated around the body with the spherical grid generated around the nose, the definition of the outer boundary was altered at the extreme forward part of the vehicle. The center of the hemispherical nose is located at (x_c, y_c, z_c) . The line determined by $B_1(x)$, the upper edge of the grid system, was projected forward all the way to $x=x_c$. Thus, the radius of the spherical grid was $r_s = B_1(x_c) - z_c$. Between $x=x_c$ and $x=x_c + 20.75 r_N$, an arbitrary point chosen forward of the canopy, all the parameters of the bi-elliptical structure varied linearly--the center from (y_c, z_c) to $(0,0)$, and the axis lengths between r_b and their values at $x_c + 20.75 r_N$. This arrangement produced a smooth variation from the bi-elliptical structure to a circular structure at $x=x_c$.

An intermediate boundary between the outer boundary and the edge of the hyperbolic mesh was prescribed in order to ensure smoothness of the

grid in the region of the bow shock wave. This boundary was chosen to have a bi-elliptical shape, so that all the circumferential lines between it and the outer boundary would be similarly shaped. Thus, all the transition between the uneven shape of the hyperbolic grid and the bi-elliptical shape of the outer grid took place in the central region (Figure 16), where the need for numerical smoothness was not as pronounced. The intermediate boundary was positioned to be a fraction $p = .30$ of the distance between the outer boundary and a shape enclosing the hyperbolic grid. The boundary of the hyperbolic grid was interrogated to determine the points of greatest extension in y , (y_1, z_1) , highest extension in z , (y_2, z_2) and the lowest extension in z , (y_3, z_3) . The center of the bi-ellipse was placed at $(0, z_1)$ with an upper z -axis length $B'_1(x) = z_2(1-p) + B_1(x)p - z_1$, and a lower z -axis length $B'_2(x) = -z_3(1-p) + B_2(x)p + z_1$. The y -axis length was $A'(x) = y_1(1-p) + A(x)p$ for $x > x_c + 20.75 r_N$ and was $A'(x)q + 1/2(B_1(x) + B_2(x)(1-q))$ for $x < x_c + 20.75 r_N$, where $q = \frac{x-x_c}{20.75 r_N}$. This ensures that the intermediate boundary approximates a circle as x approaches x_c .

The next step in performing the transfinite construction was determination of the placement of points on the intermediate and outer boundaries and specification of the stretching along the radial lines. Points were placed on the outer boundary so that the arc lengths between them were proportional to the arc lengths on the edge of the hyperbolic grid. The points on the intermediate boundary were placed in a similar fashion with an additional numerical averaging. If $s(n)$ is the accumulated arc length through the n^{th} point, proportional to the spacing on the hyperbolic grid boundary, s_{avg} is the average arc length between points, and $\sigma = 0.1$ is a smoothing parameter, then the actual arc length at the n^{th} point is $s'(n) = s(n-1) + [s(n) - s(n-1)](1-\sigma) + s_{\text{avg}}\sigma$. This smoothing relaxes the point

distribution so that it approaches an equispaced distribution. Point placement was determined for each radial line separately. In the region between the hyperbolic grid and the intermediate boundary, spacing was determined by the inverse hyperbolic sine function of Vinokur.²² The spacing at the inner boundary coincided with the outer-most spacing of the hyperbolic grid, and the spacing at the intermediate boundary was chosen to be the maximum of $0.125 r_N$ and the spacing required for an equispaced distribution along the radial line between the inner and outer boundaries. In the other region of the grid, an exponential stretching was used which matched the stretching at the intermediate boundary.

Generation of a $\xi = \text{constant}$ plane was completed by application of a Poisson averaging operator to the grid points between $j=22$ and $j=32$, a domain which included the entire middle region. This was done to promote smoothness of derivatives across the composite grid. Some typical grids can be seen in Figure 17.

Spherical Grid at the Vehicle Nose

The cylindrical coordinate system of the mesh was easily transitioned into a spherical system on the hemispherical nose. Surface points were spaced equiangularly both latitudinally and longitudinally, with radial stretching controlled by a line from the $i=7$ plane, which abuts the nose region. As mentioned above, the parameters for the composite grid are varied so that mesh in the $i=7$ plane is nearly circular. The grid points in the $i=1$ plane are the reflection in the $z=z_c$ plane of the points in the $i=2$ plane. Analytic continuation of the field variables in the ξ direction indicates that $P(k,j,1)$ and $P(k,j,3)$ are neighbors of $P(k,j,2)$ spatially (Figure 18). Due to the bilateral symmetry of the flow, all the scalar variables are equal at $P(k,j,1)$ and $P(111 - k,j,2)$, with the velocity

vectors being equal in magnitude but reflected in the $y=0$ plane. Since the spherical grid is equispaced, the flow variables need not be interpolated to set boundary conditions at $P(k,j,l)$. This type of structure can be used for any bilaterally symmetric flow. The singularity along the axis for the cylindrical-spherical system is physically avoided by the grid and boundary conditions are set across the axis of symmetry. One disadvantage of the construction is that the grid spacing along the surface of the nose is actually less than the smallest radial spacing, due to the large number of peripheral points. This is undesirable computationally, but unavoidable in a body-fitted system. The extra work required in processing was reduced in the computation by taking advantage of the data structure and only computing in the nose region when necessary.

In summary, construction of a $\xi = \text{constant}$ plane of the mesh began with the generation of a hyperbolic grid next to the surface. A composite grid was formed using transfinite interpolation from the edge of the hyperbolic grid through two outer boundaries. Lastly, a single pass of a Poisson smoothing operator was performed. All facets of the construction were chosen to promote numerical smoothness of the grid and in the ensuing computation. The mesh about the blunt nose was created as a spherical grid, juxtaposed to the forebody grid. Computational boundary conditions were provided for by setting up the grid to take advantage of analytic continuation and symmetry.

X-24C--10D BODY

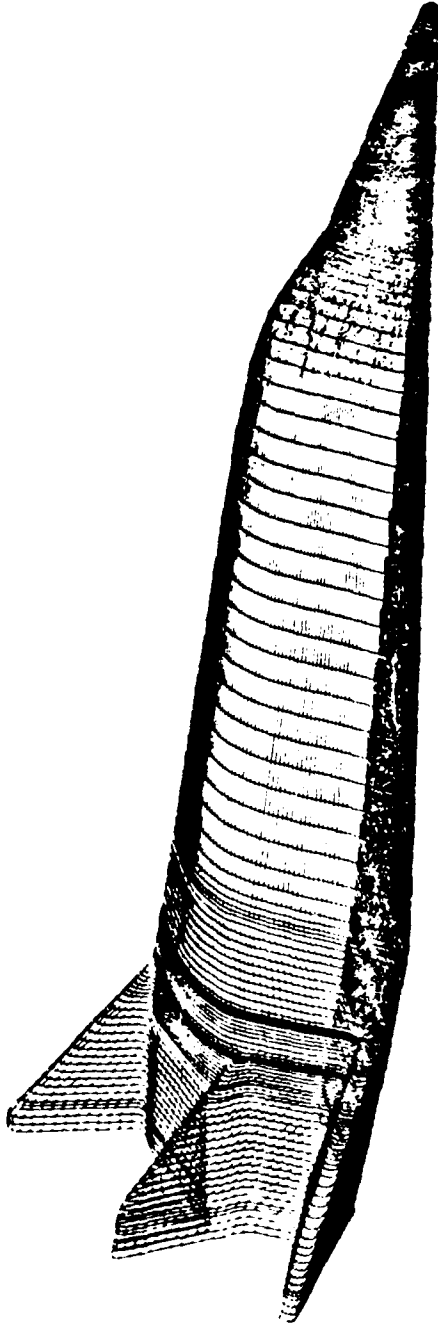
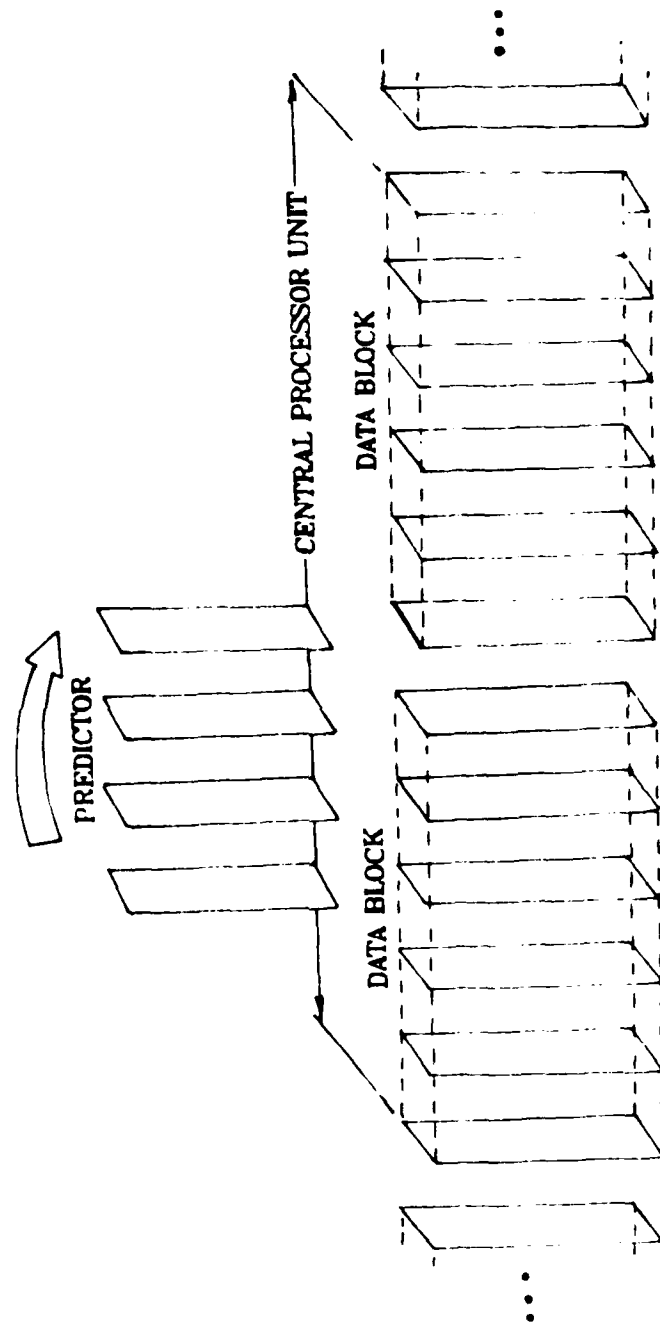


Figure 1. X24C-10D Configuration



DATA STRUCTURE AND DATA FLOW

Figure 2. Data Structure and Data Flow

SURFACE PRESSURE

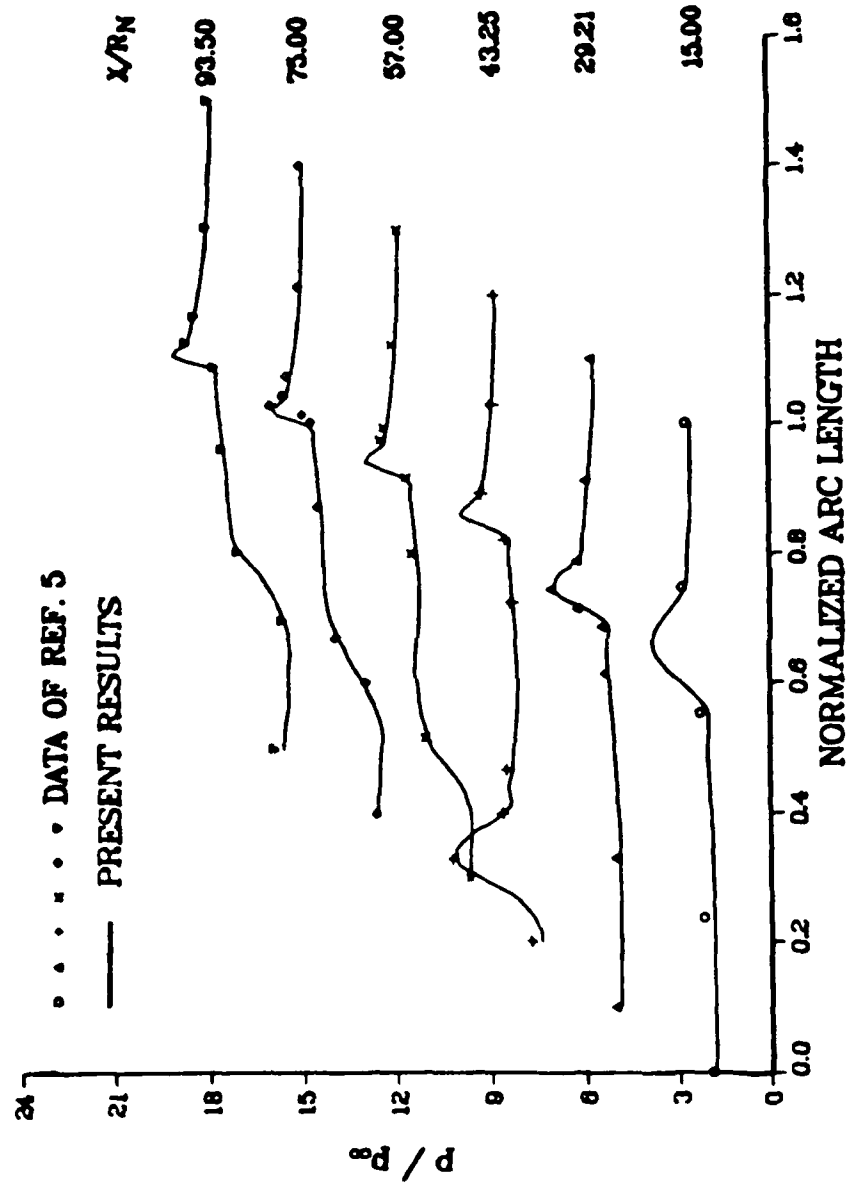


Figure 3. Peripheral Surface Pressure Distributions of the Forebody

SURFACE PRESSURE

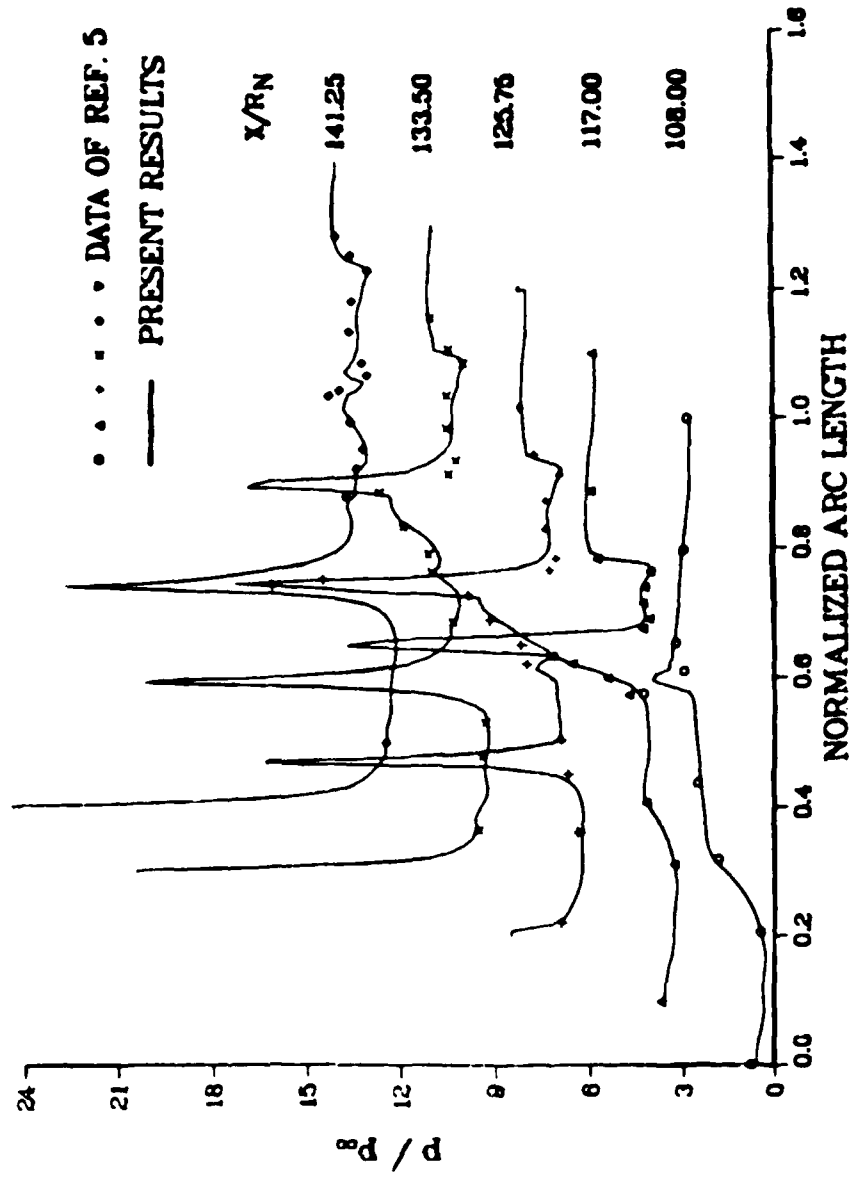


Figure 4. Peripheral Surface Pressure Distributions of the Afterbody

Center Fin Surface Pressure

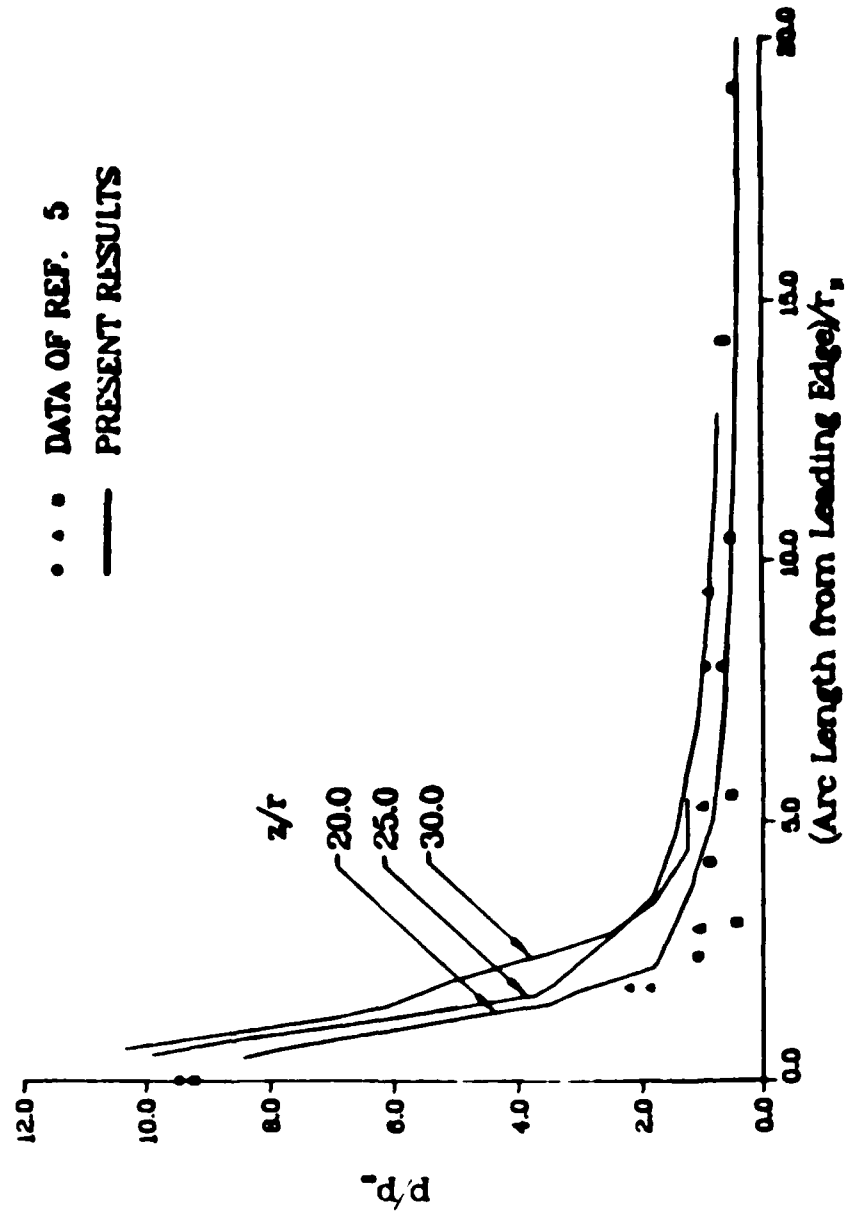


Figure 5. Surface Pressure Distribution on the central fin

COMPARISON WITH PIVOT PRESSURE SURVEY

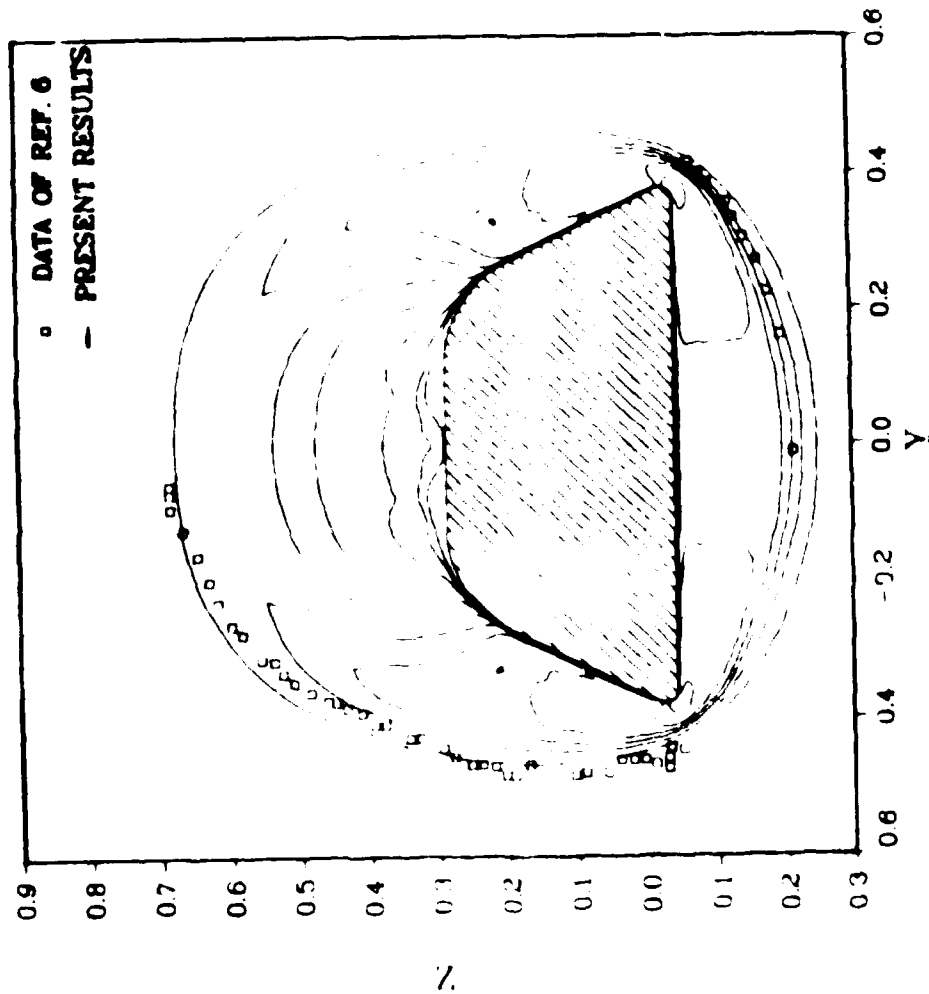


Figure 6. Comparison of Pivot Pressure Survey ($X R_D = 108$)

HEAT TRANSFER

. DATA OF REF. 6 AND 7

— PRESENT RESULTS

X/R_N

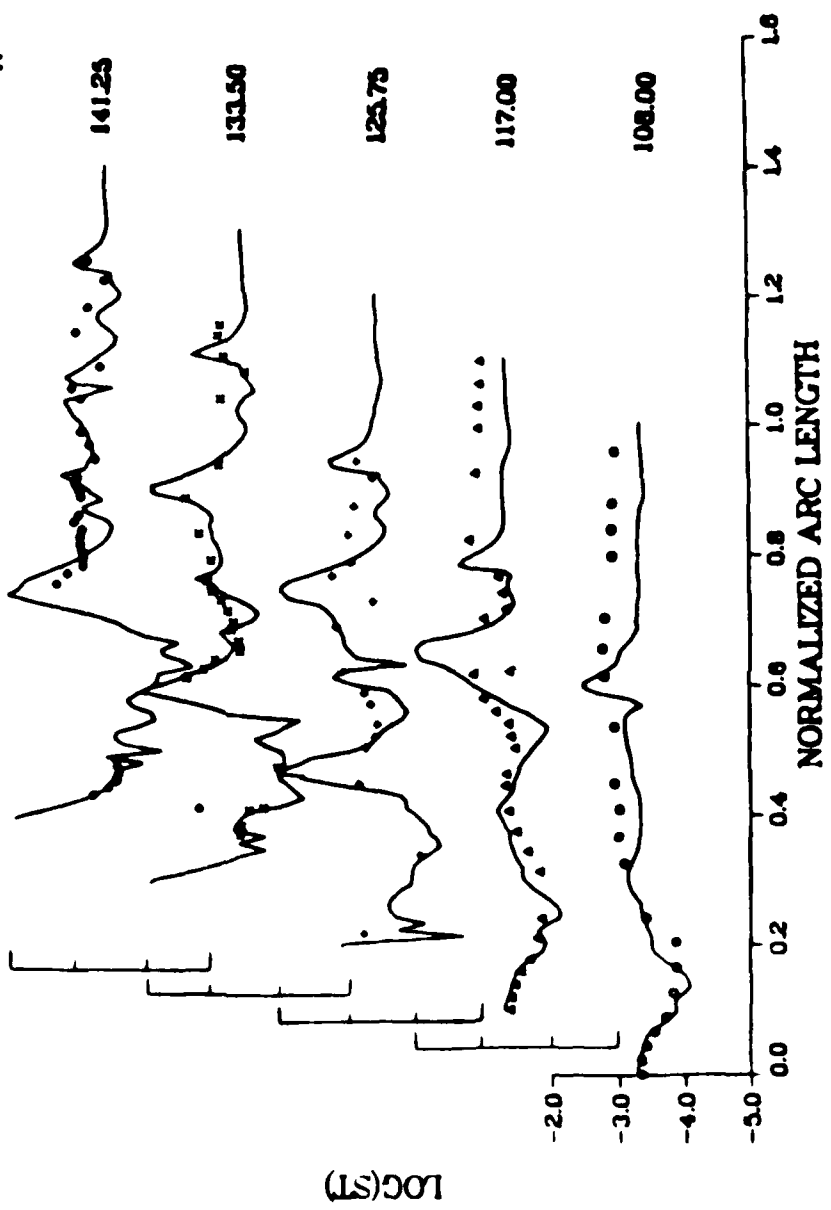


Figure 7. Peripheral Heat Transfer Distributions

COMPARISON OF PNS AND NAVIER-STOKES

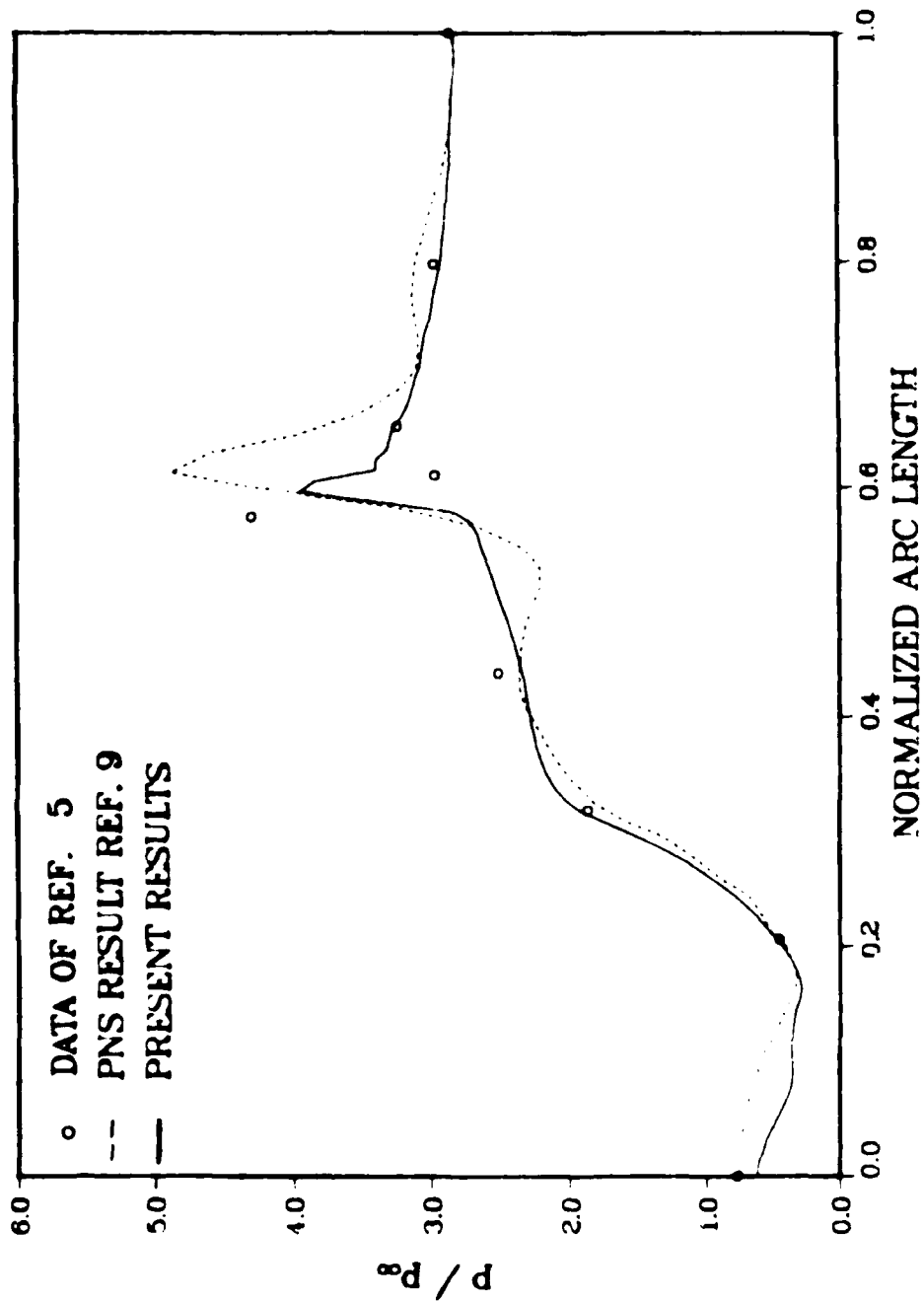


Figure 8. Comparison of Surface Pressure Distributions at $X/R_n = 105.0$

HEAT TRANSFER COMPARISON

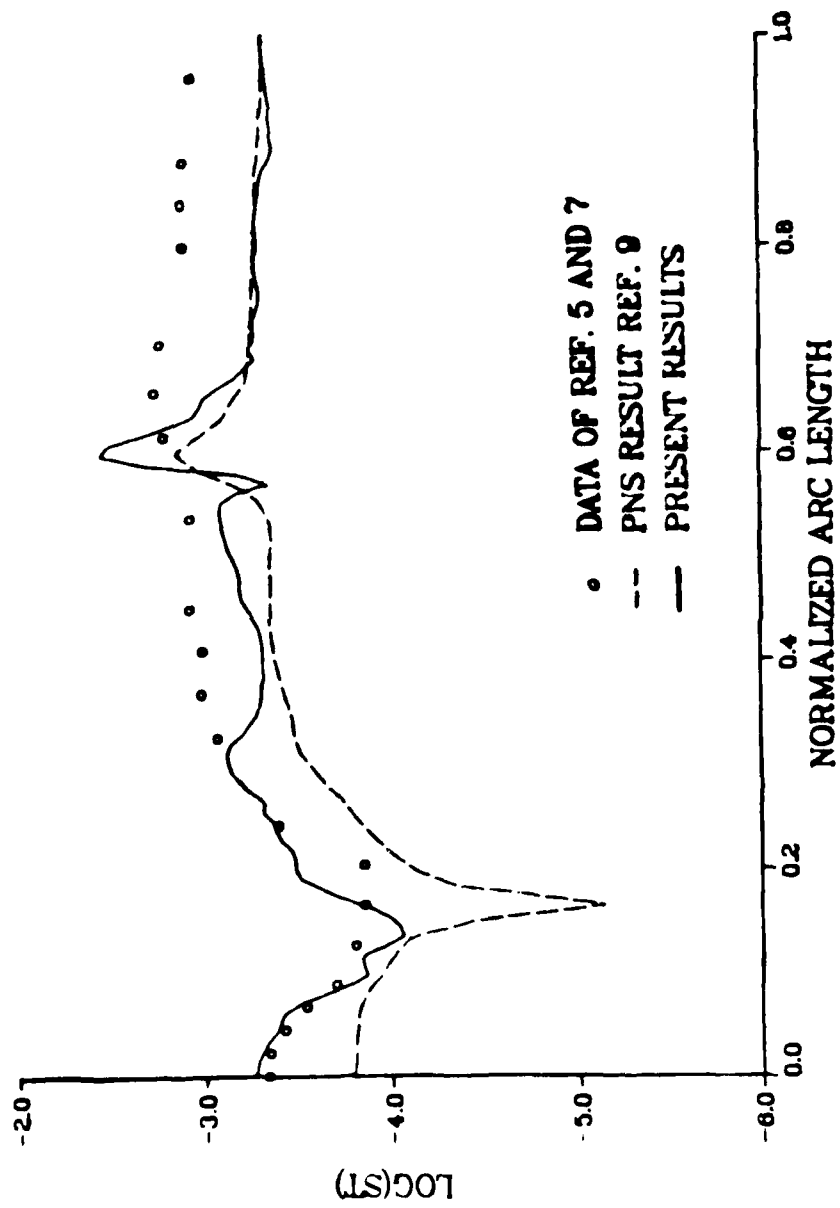


Figure 9. Comparison of Heat Transfer at $X/R_n = 108.0$

Axial Surface Pressure Variation

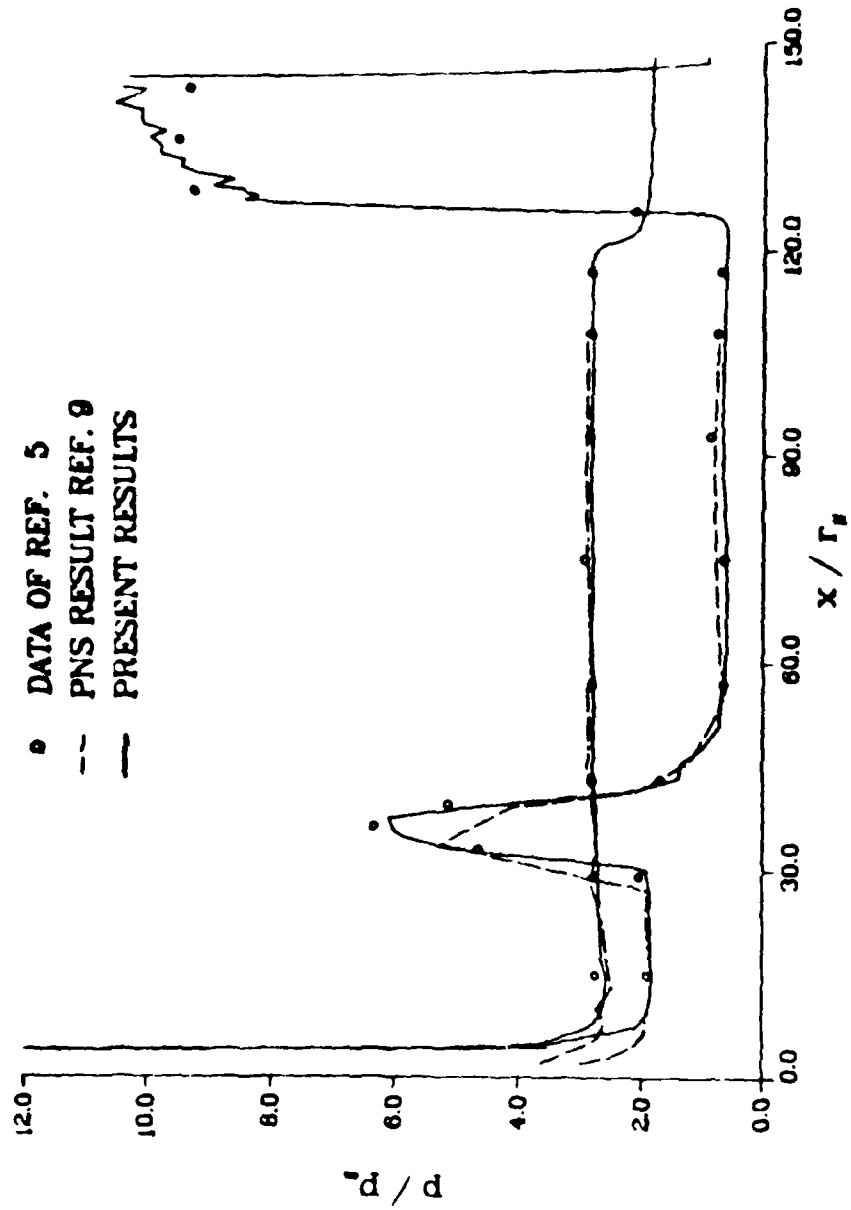
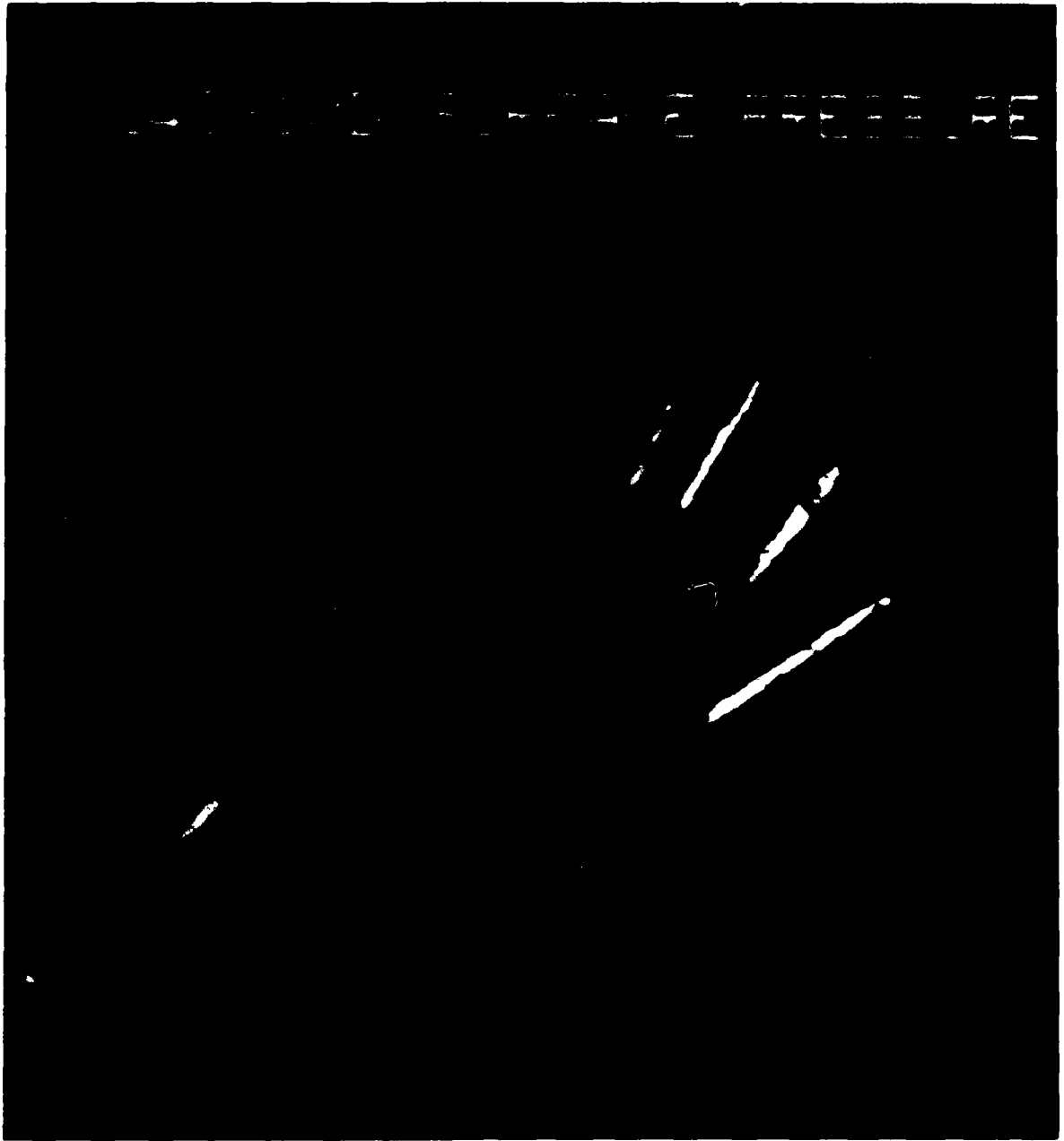


Figure 10. Comparison of Streamwise Surface Pressure Distributions



SHANG AND SCHERR - PLATE 1
Surface pressure contours

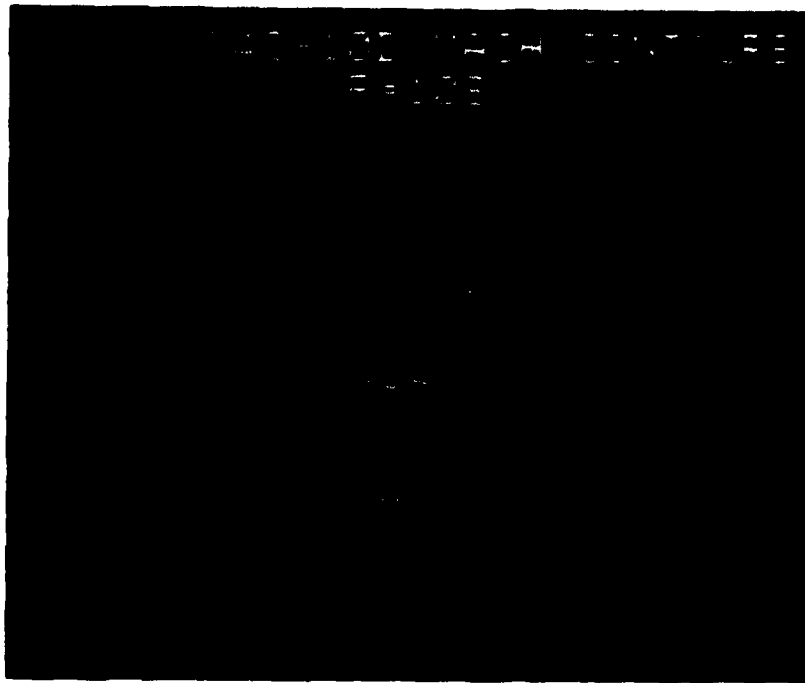
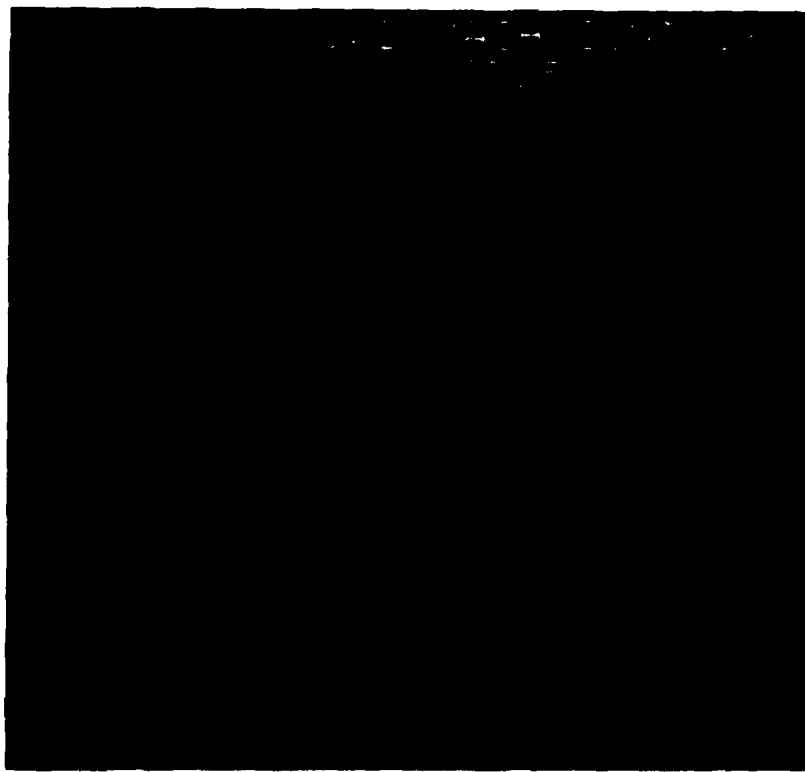
Figure 11. Surface Pressure Contour

X-24C-100 HEAT TRANSFER



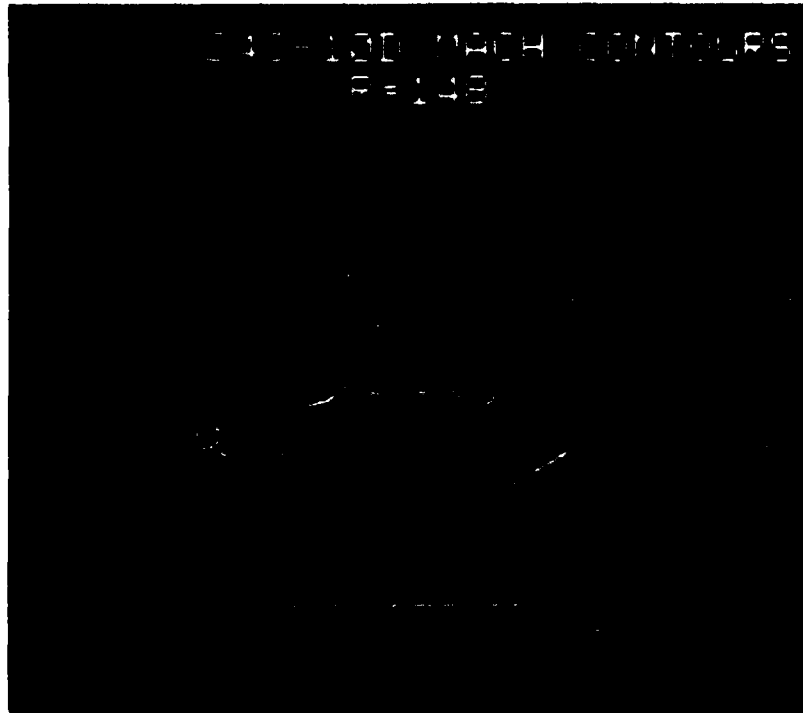
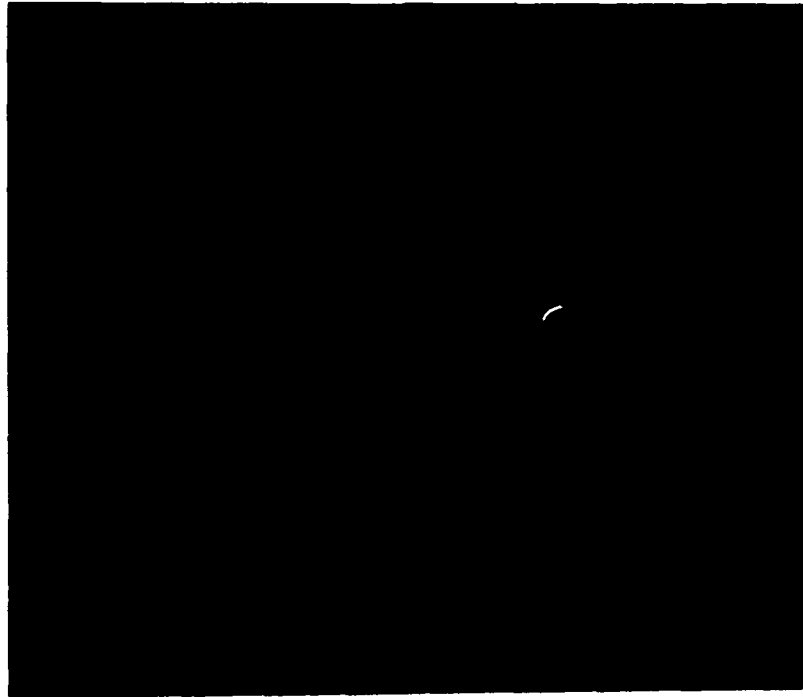
SHANG AND SCHLERK - PLATE 2
Heat transfer contours

Figure 12. Surface Heat Transfer
Contours



SHANG AND SCHERR: PLATE 3
Cross-sectional Mach contours. (a) $x/r = 38.5$. (b) $x/r = 108$ (continue)

Figure 13. Cross-sectional Mach Number
Contours
(continue)



SHANG AND SCHERR: PLATE 3
Cross-sectional Mach contours, (c) $x/r = 125.6$, (d) $x/r = 148$ (concluded).

Figure 13. Cross-sectional Mach Number
Contours
(concluded)

Symmetry Plane Mach Contours

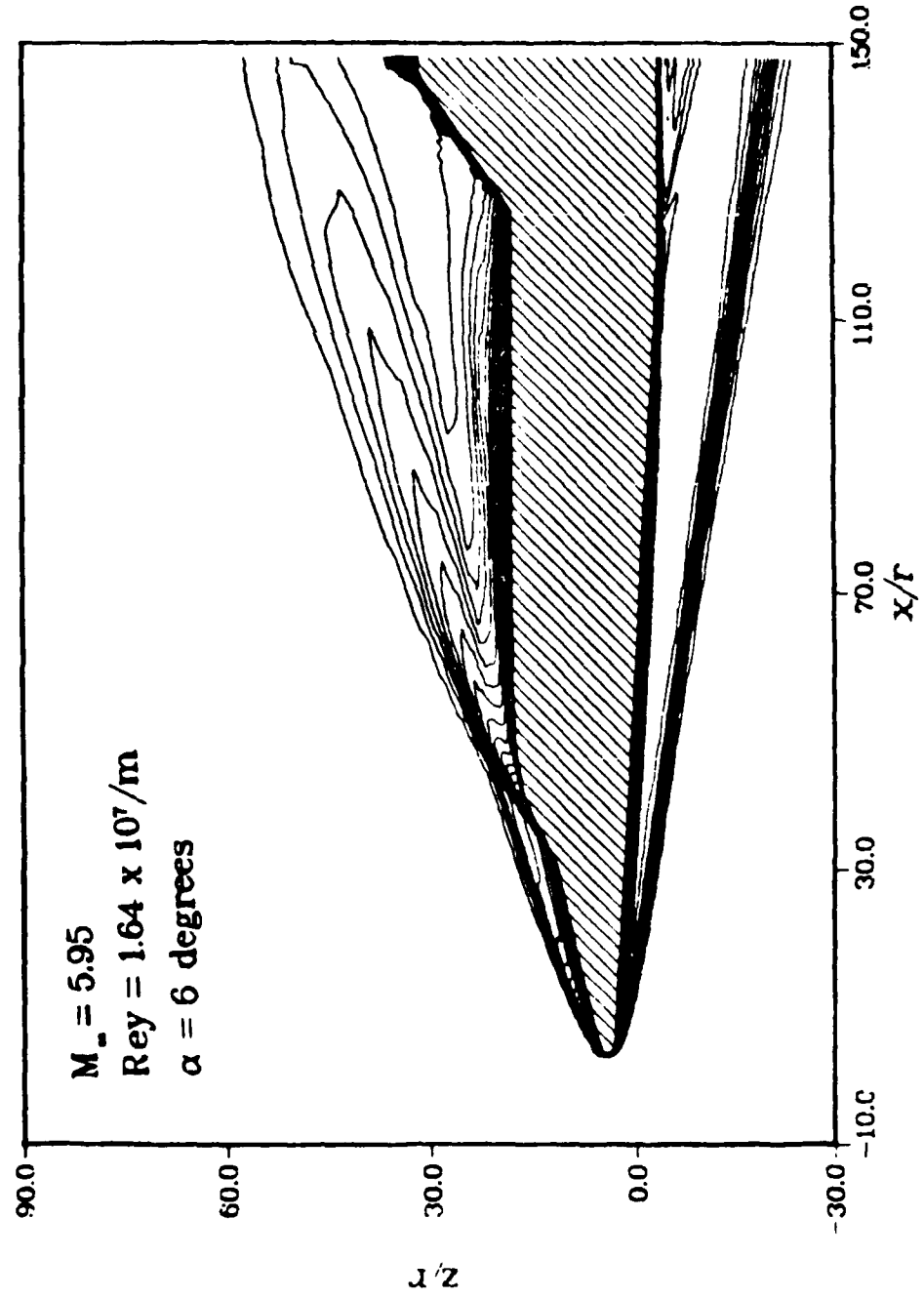


Figure 14. Mach Number Contour Projected on the Plane of Symmetry

SURFACE STREAMLINE PATTERN

$M_\infty = 5.96$
 $Re_\gamma = 1.64 \times 10^7 / \text{in}$
 $\alpha = 6 \text{ degrees}$

	C_L	C_D	L/D
Experimental Data	3.676×10^{-2}	3.173×10^{-2}	1.158
Numerical Result	3.503×10^{-2}	2.960×10^{-2}	1.183
Error (percent)	4.71	6.71	2.16

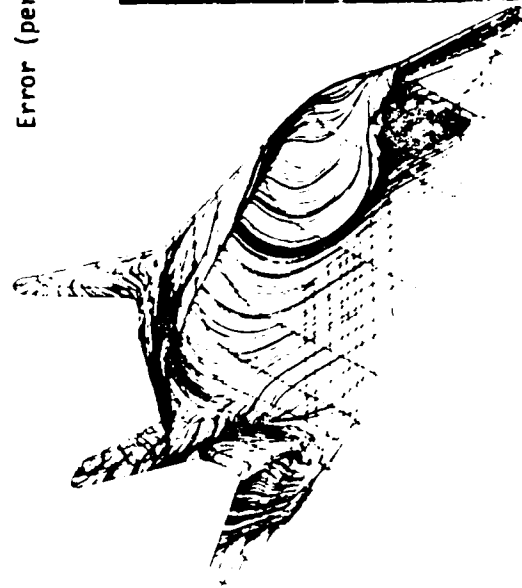


Figure 15. Surface Streamline Pattern

**COMPOSITE GRID SYSTEM
HYPERBOLIC AND TRANS-FINITE**

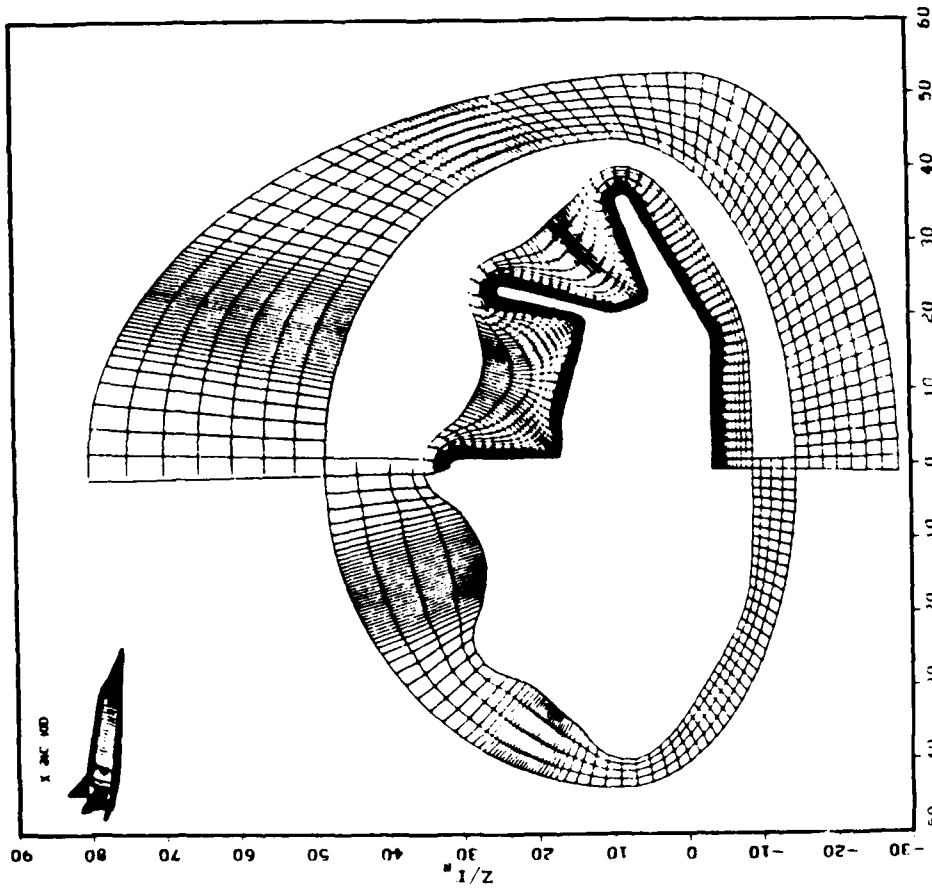


Figure 16. Compositing Grid Structure by Hyperbolic and Trans-Finite Schemes

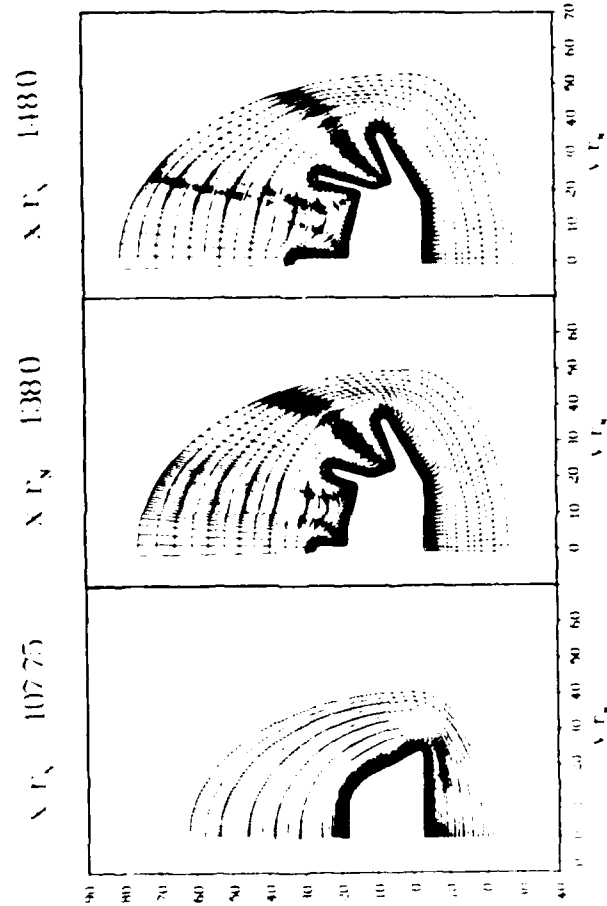


Figure 17. Typical Grid Systems in Selected Planes

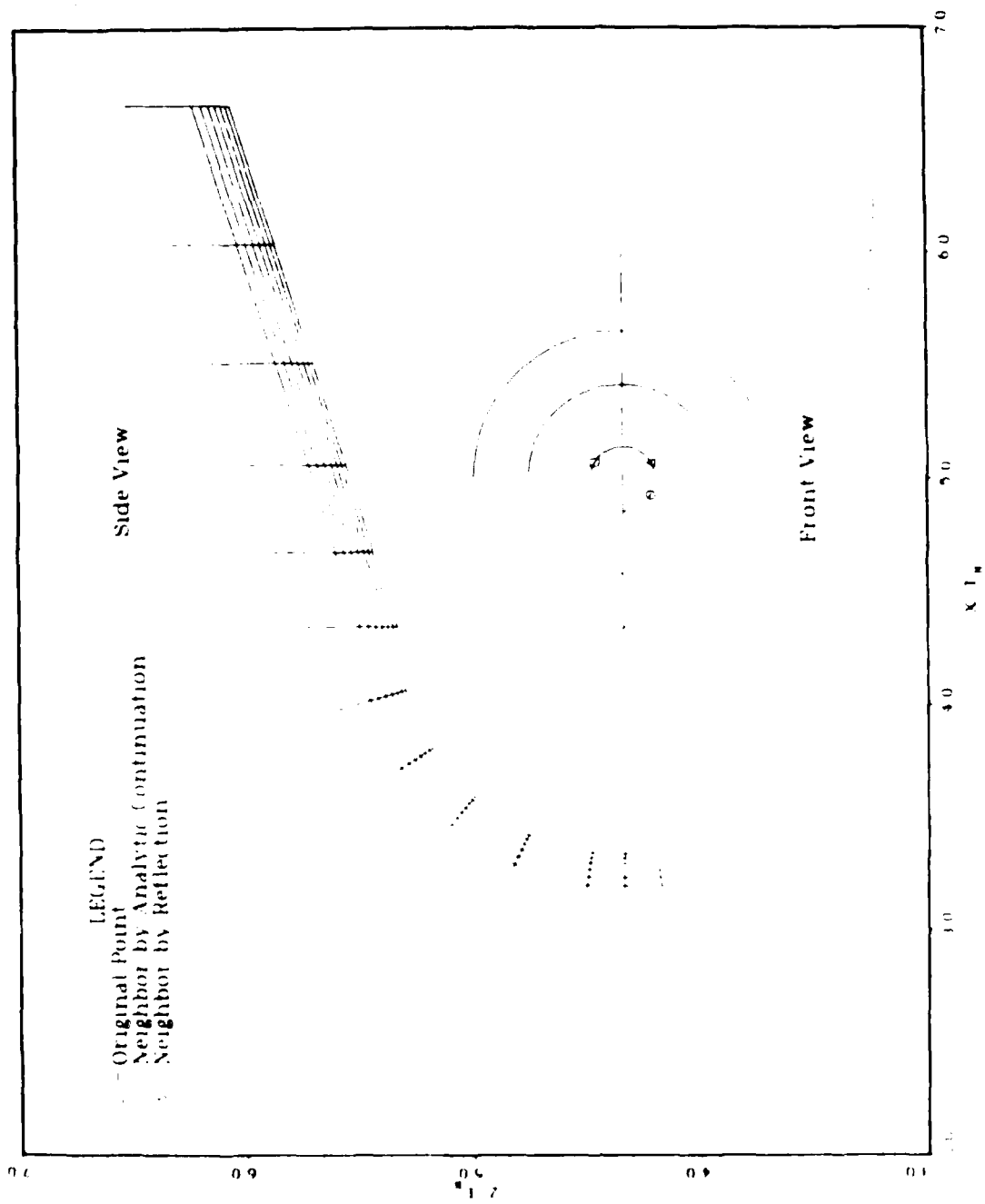


Figure 18. Detailed Grid Construction in the Nose Region

END

9-87

DTIC